International Forum on Aeroelasticity and Structural Dynamics
IFASD 2024
17-21 June 2024, The Hague, The Netherlands

# COMPARATIVE ANALYSIS OF FLIGHT MANEUVER LOADS BETWEEN FLEXIBLE AND RIGID AIRCRAFT

**Eduardo A. M. Pinto**[1], **Flávio L. Cardoso-Ribeiro**[1], **Fernando J. O. Moreira**[2]

[1]Instituto Tecnológico de Aeronáutica
Praça Marechal do ar Eduardo Gomes, 50, 12228-900, São José dos Campos, Brazil
eduardomeloeng@gmail.com
flaviocr@ita.br

[2]EMBRAER S.A.
Av. Brigadeiro Faria Lima, 2170, 12227-901, São José dos Campos, Brazil
fernando.moreira@embraer.com.br

**Keywords:** Internal loads, inertially coupled equations, force summation method, quasi-steady VLM, wing, horizontal tail

**Abstract:** The analysis of aircraft loads during flight maneuvers plays a pivotal role in ensuring structural integrity, safety, design of lighter structures and more fuel-efficient vehicles. This study focuses on a comparative analysis of internal load diagrams and flight parameters time histories for a flexible aircraft and its rigid-body counterpart, emphasizing the impact of structural flexibility on flight dynamics and loads during flight maneuvers. The research employs a dynamically-coupled formulation for the flexible model, considering small deformations and inertially coupled equations of motion. The aerodynamic loads are calculated with a quasi-steady VLM model, and the structural dynamics is represented by a linear FEM model. The rigid-body model is obtained by neglecting structural flexibility, setting the number of elastic modes to zero. To calculate the internal loads, the force summation method is employed. Three maneuvers from CS-25 specifications are simulated: the symmetrical unchecked and checked maneuvers, and the roll maneuver. For the unchecked and roll maneuvers, the flexible model exhibits a slightly slower response and reduced wing and horizontal tail loads compared to the rigid model. In the checked maneuver, the flexible model displays nuanced differences in flight dynamics and horizontal tail loads, computing higher absolute TMY values, and higher SLZ and BMX loads at the instant of maximum positive FZTH, while the rigid-body model presented higher absolute values of SLZ and BMX. Regardless of the obtained variations, the study emphasizes the importance of considering structural flexibility in analyzing flight maneuver loads and the need for more precise and efficient methods to address the evolving landscape of aircraft design.

## 1 INTRODUCTION

During aircraft design, engineers calculate load envelopes to determine critical design loads for airframe structures and systems, and for certification purposes [1]. Load analysis is iterative, becoming more accurate as the design progresses. To calculate loads from flight maneuvers, gusts, and turbulence encounters, engineers use flight dynamics models that vary in complexity. These can range from simple single degree of freedom (DOF) models for specific maneuvers [2, 3] to complex models considering six DOF for rigid-body dynamics and additional DOF for structural dynamics.

In aerospace industry, different models are generally developed to analyze flight maneuvers and gust/turbulence encounter loads. Maneuver analysis typically uses time-domain simulations with nonlinear equations of motion (EOM), possibly simplifying by ignoring or adjusting aerodynamic coefficients for accounting structural flexibility. However, gust analysis often uses linear equations in the frequency domain to include structural dynamics and unsteady aerodynamic effects [1].

The need for safer and energy-efficient aircrafts with lighter structures and wings with a higher aspect ratio increases structural flexibility, decreasing the frequency separation between rigid-body and elastic modes. This interaction can affect flight dynamics, necessitating more precise load analysis methods.

The nonlinear EOM for an elastic airplane is derived in [4], assuming simplifying assumptions, such as small structural deformations and displacements, disregarding any variation of the inertia tensor due to structural deformation, therefore, there is no inertial coupling between the rigid-body and elastic DOF, which are coupled only through aerodynamic and propulsive forces and moments. A similar model is developed in [5] for modeling the flight dynamics of a slight flexibe, high aspect ratio aircraft, where a flight campaign demonstrated excellent agreement with the simulations, and aeroelastic analysis presented difference of 5% in the flutter speed prediction with the commercial tool ZAERO.

Reference [6] presents a comprehensive study of the flight dynamics of the GNBA (*generic narrow-body airliner*), an aircraft developed within the context of this research. The thesis investigates the application of three distinct body-axis systems, all assuming small deformations and inertial coupling effects. In assessing the incremental aerodynamics associated with the airframe's flexibility, unsteady *Doublet Lattice* (DLM) and quasi-steady *Vortex Lattice* (VLM) methods are employed. An interested conclusion of this work is that quasi-steady VLM model adequately predicts the rigid-body flight dynamic modes for the flexible aircraft, therefore, for a slightly flexible aircraft, the quasi-steady VLM model may suffice to capture the influence of flexibility on flight dynamics.

Flight loads analysis assuming a rigid aircraft is addressed by [2, 3, 7]. The impact of structural displacements in flight loads is commented in [7]. Flight loads analysis for an aeroelastic vehicle is addressed by [1, 8–14]. Different formulations for internal loads recovery are derived: Mode Displacement Method (MDM) [8], Mode Acceleration Method (MAM) [8], and the Force Summation Method (FSM) [1, 9]. These three methods yield theoretically identical results when a sufficient number of elastic modes are considered [10].

A comparison between flight loads of a flexible aircraft obtained with inertially uncoupled EOM and inertially coupled EOM is presented in [1]. The FSM is selected for calculating nodal loads due to its superior convergence behavior. A structural model developed using the finite element method (FEM) is available to represent the structural dynamics. The aerodynamic loads are obtained through a combination of quasi-steady forces based on available database and unsteady effects calculated with DLM method. A comparison of shear loads and nodal forces between the intertially coupled and uncoupled formulations are presented for a roll maneuver simulation. The primary conclusion drawn from this analysis underscores the significance of inertial coupling on both local and integrated loads, particularly noticeable in components with large concentrated masses, like the engines.

The aforementioned quasi-steady VLM was originally formulated by [15]. This method in-

volves dividing the lifting surface into numerous panels distributed both chordwise and spanwise. Aerodynamic forces are computed at each panel by employing horseshoe vortex, applying appropriated boundary conditions. This reference also addresses how to deal with the effects of the modification of lifting surface camber due to structural elasticity.

The DLM method, introduced by [16], represents an extension of Headman's VLM [15] to unsteady and oscillatory potential flows. Its use is widespread in the aeronautical industry for the certification of aircraft with respect to aeroelastic stability [17].

According to [18], not considering the unsteady aerodynamic effects is justified whenever the elastic modal periods are long compared to the rate of change of the pressure distributions over the lifting surfaces. Consequently, a flexible aircraft model based on quasi-steady aerodynamics may be adequate to capture the aerodynamic loads during flight maneuvers as described in subpart C of CS-25 specifications [19], but it is not adequate to simulate discrete gusts with high frequency gradients and continuous gusts.

This work focuses on a comparative analysis of internal load diagrams for the same aircraft and flight maneuvers, utilizing two distinct models. The first model employs equations of motion for a flexible aircraft, while the second model assumes only rigid-body motion. The comparisons are made for three maneuvers from CS-25 specifications [19] and the internal load diagrams are presented for wing and horizontal tail, enabling an assessment of the influence of flexibility on typical flight maneuver loads.

The GNBA aircraft, developed in [6], is employed as a platform for the analysis. This aircraft is a representative model of a commercial airplane with seating capacity for 130 passengers, developed to study the effects of structural flexibility on the flight dynamics. The flight dynamics of the flexible aircraft are modeled with a dynamically-coupled formulation, assuming small deformations and inertially coupled EOM, and the flight dynamics of the rigid aircraft are modeled with a 6 DOF equations of motion. A quasi-steady aerodynamic model is employed to calculate the aerodynamic loads, and the FSM equations are implemented to recovery of structural loads.

## 2 EQUATIONS OF MOTION

The flight dynamics model employed in this work was originally developed as part of a coursework activity in the ITA's AB-276 course in 2020 [17]. In this course, a flight dynamics model of a flexible aircraft was developed applying some simplifying assumptions that made the equations of motion inertially uncoupled. The EOM are augmented with the inertial coupling effects, according to [1]. These equations are presented in Section 2.1. The EOM for the rigid aircraft are presented in Section 2.2.

The inertial reference system is assumed as a tangential Earth-fixed reference frame. The vehicle frame is assumed as a body-fixed forward-right-down coordinate system. The position of a mass element ($dm_j$), the origin of the inertial ($I$) and body ($O$) reference systems, and the instantaneous center of mass ($C$), as well as the body reference system, are presented in Figure 1.

Figure 2 presents the position vectors of a grid point and a mass element in reference and deformed conditions.

The position vector of the origin of the body coordinate system is $\boldsymbol{R_O} = \begin{bmatrix} x & y & -h \end{bmatrix}^T$. The

velocity vector of the origin of the body coordinate system ($\boldsymbol{V_b} = \begin{bmatrix} u & v & w \end{bmatrix}^T$) is related to the inertial coordinate system using the following equation:

$$\dot{\mathbf{R}}_\mathbf{O} = \left( \begin{bmatrix} 1 & 0 & 0 \\ 0 & \cos\phi & \sin\phi \\ 0 & -\sin\phi & \cos\phi \end{bmatrix} \begin{bmatrix} \cos\theta & 0 & -\sin\theta \\ 0 & 1 & 0 \\ \sin\theta & 0 & \cos\theta \end{bmatrix} \begin{bmatrix} \cos\psi & \sin\psi & 0 \\ -\sin\psi & \cos\psi & 0 \\ 0 & 0 & 1 \end{bmatrix} \right)^T \mathbf{V_b} \quad (1)$$

The orientation of the body coordinate system is defined using the Euler angles $\boldsymbol{\Theta} = \begin{bmatrix} \phi & \theta & \psi \end{bmatrix}^T$. The angular velocity vector is defined as $\boldsymbol{\omega_b} = \begin{bmatrix} p & q & r \end{bmatrix}^T$.

The time derivative of the Euler angles are related to the angular velocity vector using the following equation:

$$\dot{\boldsymbol{\Theta}} = \begin{bmatrix} 1 & 0 & -\sin\theta \\ 0 & \cos\phi & \sin\phi\cos\theta \\ 0 & -\sin\phi & \cos\phi\cos\theta \end{bmatrix}^{-1} \boldsymbol{\omega_b} \quad (2)$$

### 2.1 Flexible Aircraft

The equations of motion outlined in this section are derived from the AB-276 course [17] and reference [1]. It is not the scope of this work to derive the EOM from first principles. This

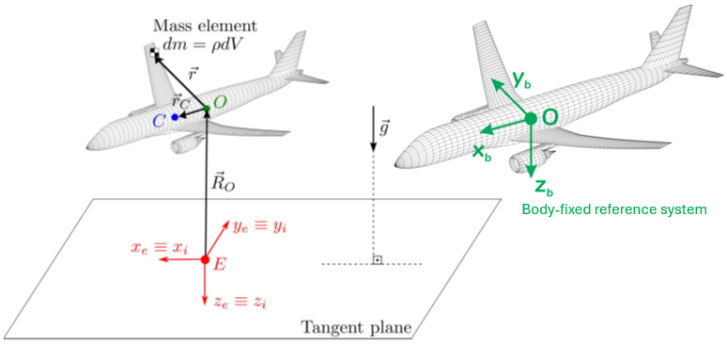


Figure 1: Position of relevant points from the inertial reference system and body-fixed reference system for flight dynamics, adpated from [17].

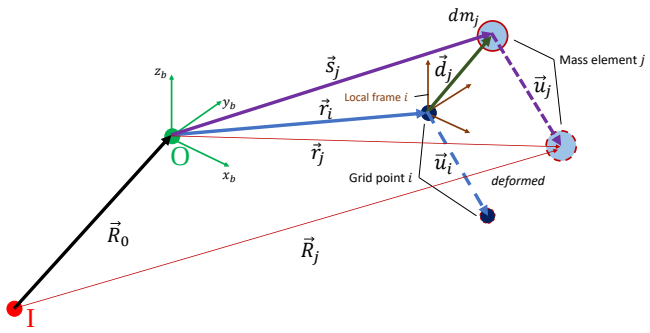


Figure 2: Location of a grid point and a mass element in reference and deformed condition.

section exclusively provides an overview of the pertinent assumptions and the final equations. The detailed derivation of theses equations is demonstrated in [1, 4, 6].

The development of the EOM relies on the following key assumptions:

**Assumption 1:** The structural deformation is assumed sufficiently small, such that linear elastic theory is valid.

**Assumption 2:** A set of normal vibration modes resulting from a free-free modal analysis are available.

**Assumption 3:** The aircraft is described as a collection of lumped mass elements, with an associated mass $m_i$ and inertia tensor $\boldsymbol{J_i}$.

**Assumption 4:** The mass density of each element is constant.

### *2.1.1 Rigid-body DOF*

Equations 3 and 4 determine the Newton's second law applied at a point located at the origin of the body axes.

$$\dot{\mathbf{p}}_\mathbf{b} + \widetilde{\boldsymbol{\omega}_b}\mathbf{p}_\mathbf{b} = \boldsymbol{F_b^{ext}} \tag{3}$$

$$\dot{\mathbf{h}}_{\mathbf{O,b}} + \widetilde{\boldsymbol{\omega}_b}\mathbf{h}_{\mathbf{O,b}} = \widetilde{\mathbf{p}_\mathbf{b}}\mathbf{V}_\mathbf{b} + \boldsymbol{M_{O,b}^{ext}} \tag{4}$$

Where $\mathbf{p_b}$ and $\mathbf{h_{O,b}}$ are the linear and angular momentum, respectively. $\boldsymbol{F_b^{ext}}$ and $\boldsymbol{M_{O,b}^{ext}}$ are the external forces and moments, respectively, that can be categorized into gravitational and non-conservative forces and moments, the last encompassing the aerodynamic and propulsive forces and moments. The skew-symmetric matrix operator applied to a vector $\boldsymbol{v} = \begin{pmatrix} v_x & v_y & v_z \end{pmatrix}^T$ provides:

$$\widetilde{\mathbf{v}} = skew(\mathbf{v}) = \begin{bmatrix} 0 & -v_z & v_y \\ v_z & 0 & -v_x \\ -v_y & v_x & 0 \end{bmatrix} \tag{5}$$

Therefore, the operation $\widetilde{\mathbf{v_1}}\mathbf{v_2} = \mathbf{v_1} \times \mathbf{v_2}$.

The linear momentum expression (Equation 3) can be further expanded, obtaining:

$$\begin{gathered} m\dot{\mathbf{V}}_\mathbf{b} - m(\widetilde{\mathbf{s_{C,b}}} + \widetilde{\mathbf{u_{C,b}}})\dot{\omega}_\mathbf{b} + m\boldsymbol{D_{C,b}}\ddot{\boldsymbol{q}} = \\ = \boldsymbol{F_b^{ext,nc}} + m\mathbf{g_b} - 2m\widetilde{\boldsymbol{\omega}_b}\boldsymbol{D_{C,b}}\dot{\boldsymbol{q}} - m\widetilde{\boldsymbol{\omega}_b}\mathbf{V_b} - m\widetilde{\boldsymbol{\omega}_b}^2\mathbf{s_{C,b}} - m\widetilde{\boldsymbol{\omega}_b}^2\boldsymbol{D_{C,b}}\boldsymbol{q} \end{gathered} \tag{6}$$

Where $\boldsymbol{u_{C,b}} = \boldsymbol{D_{C,b}}\boldsymbol{q}$, $\boldsymbol{D_{C,b}} = \frac{1}{m}\int_V \rho N_b(\boldsymbol{r_i})dV$, $\mathbf{s_{C,b}}$ is the position vector of the center of mass of the undeformed aircraft in body axes, $m$ is the aircraft mass and $\mathbf{g_b}$ is the vector of gravitational acceleration.

The angular momentum expression (Equation 4) can be further expanded, obtaining:

$$\begin{gathered} m(\widetilde{\boldsymbol{\omega_b}} + \widetilde{\mathbf{u}_{\mathbf{C,b}}})\dot{\mathbf{V}}_{\mathbf{b}} + (\boldsymbol{J_{O,b}} + \Delta\boldsymbol{J_{O,b}})\dot{\omega}_{\mathbf{b}} + \overline{\boldsymbol{M}}\ddot{\boldsymbol{q}} + \int_V \rho\widetilde{\mathbf{u}}_{\mathbf{j}}\ddot{\mathbf{u}}_{\mathbf{j}}dV = \\ = \boldsymbol{M}_{\boldsymbol{O,b}}^{\boldsymbol{ext,nc}} + m(\widetilde{\mathbf{s}_{\mathbf{C,b}}} + \widetilde{\mathbf{u}_{\mathbf{C,b}}})\mathbf{g}_{\mathbf{b}} - m(\widetilde{\boldsymbol{\omega_b}} + \widetilde{\mathbf{u}_{\mathbf{C,b}}})\widetilde{\boldsymbol{\omega_b}}\mathbf{V}_{\mathbf{b}} - \Delta\dot{\boldsymbol{J}}_{\boldsymbol{O,b}}\boldsymbol{\omega_b} \\ -\widetilde{\boldsymbol{\omega_b}}(\boldsymbol{J_{O,b}} + \Delta\boldsymbol{J_{O,b}})\boldsymbol{\omega_b} - \widetilde{\boldsymbol{\omega_b}}\int_V \rho\widetilde{\mathbf{s}}_{\mathbf{j}}\dot{\mathbf{u}}_{\mathbf{j}}dV - \widetilde{\boldsymbol{\omega_b}}\int_V \rho\widetilde{\mathbf{u}}_{\mathbf{j}}\dot{\mathbf{u}}_{\mathbf{j}}dV \end{gathered} \tag{7}$$

Where $\mathbf{u}_{\mathbf{C,b}}$ is the position vector of the center of mass of the deformed aircraft in body axes and $\overline{\boldsymbol{M}} = \int_V \rho\widetilde{\boldsymbol{s_j}}N_b(\boldsymbol{r_i})dV$.

The mean axes, detailed in [4, 6, 17], serve as the body axes employed in the simulations conducted in this study. The practical mean-axis constraints applied to the linear and angular momentum equations are:

$$\begin{aligned} \boldsymbol{D_{C,b}q} &= 0 \\ \overline{\boldsymbol{M}}\boldsymbol{q} &= 0 \end{aligned} \tag{8}$$

These constraints ensure that the instantaneous center of mass $C$ of the flexible aircraft does not move with respect to the mean-axis reference frame.

For the unrestrained aircraft undergoing unforced vibrations and without structural damping, the EOM that dictate the elastic DOF are given by:

$$\mathbf{M}\ddot{\boldsymbol{q}} + \mathbf{K}\boldsymbol{q} = 0 \tag{9}$$

Where $\boldsymbol{M}$ is the aircraft mass matrix and $\boldsymbol{K}$ is the stiffness matrix. It is assumed the following solution:

$$\boldsymbol{q} = \boldsymbol{q_j}e^{i\omega_j t} \tag{10}$$

Resulting in the subsequent eigenvalue problem:

$$(\mathbf{M}^{-1}\mathbf{K} - \boldsymbol{\omega_j}^2\boldsymbol{I_n})\boldsymbol{q_j} = 0 \tag{11}$$

According to [20], the following are assumed:

- The eigenvalues $\omega_j^2$ are positive real numbers, that represents the natural frequencies $\omega_n$ of each mode;
- The eigenvectors $\boldsymbol{q_j}$ are real column matrices representing the mode shapes of the unrestrained aircraft;
- The eigenvectors are orthogonal with respect to $\mathbf{M}$ and $\mathbf{K}$.

The $n$ - 6 deformation mode shapes can be collected as columns of a modal matrix $\boldsymbol{\Phi_m}$:

$$\boldsymbol{\Phi_m} = \begin{bmatrix} \boldsymbol{q_1} & \boldsymbol{q_2} & \dots & \boldsymbol{q_{n-6}} \end{bmatrix} \tag{12}$$

With these matrices, the transformation from the physical to generalized coordinates are given by:

$$\boldsymbol{q}(t) = \boldsymbol{\Phi_m}\boldsymbol{\eta}(t) \tag{13}$$

To eliminate the summation over the grid points in solving the integrals presented in Equation 7, a formulation that relies on a set of constant matrices multiplied by the mode shapes are developed in [1]. With this approach, a enhanced computational efficiency is achieved.

The expression for the incremental inertia matrix is provided below:

$$\Delta \boldsymbol{J_{O,b}} = -\langle \boldsymbol{\eta}^T \widehat{\boldsymbol{B}}_{\boldsymbol{jk}} \boldsymbol{\eta} \rangle - \langle \widehat{\boldsymbol{C}}_{\boldsymbol{jk}} \boldsymbol{\eta} \rangle \tag{14}$$

The notation $\langle ... \rangle$ is introduced to shorten the summation over the matrix elements:

$$\begin{aligned} \langle (...)_{jk} \rangle &= \sum_{j=1}^{3} \sum_{k=1}^{3} (...)_{jk} \boldsymbol{e_j} \boldsymbol{e_k}^T \\ \langle (...)_{j} \rangle &= \sum_{j=1}^{3} (...)_{j} \boldsymbol{e_j} \end{aligned} \tag{15}$$

where $\boldsymbol{e}$ denotes a unit vector, with it's $j$th or $k$th component of the column matrix equal to 1, while all the other components are null.

The time derivative of the incremental inertia matrix is calculated with the following equation:

$$\Delta \dot{\boldsymbol{J}}_{\boldsymbol{O,b}} = -\langle \dot{\boldsymbol{\eta}}^T \widehat{\boldsymbol{B}}_{\boldsymbol{jk}} \boldsymbol{\eta} \rangle - \langle \boldsymbol{\eta}^T \widehat{\boldsymbol{B}}_{\boldsymbol{jk}} \dot{\boldsymbol{\eta}} \rangle - \langle \widehat{\boldsymbol{C}}_{\boldsymbol{jk}} \dot{\boldsymbol{\eta}} \rangle \tag{16}$$

The integrals defined in Equation 7, featuring the cross product terms $\widetilde{\boldsymbol{u_j}} \dot{\boldsymbol{u}}_{\boldsymbol{j}}$ and $\widetilde{\boldsymbol{u_j}} \ddot{\boldsymbol{u}}_{\boldsymbol{j}}$, are represented by the matrices $\mathbf{h}$ and $\dot{\mathbf{h}}$, respectively, as presented in the following equations:

$$\begin{aligned} \mathbf{h} &= \int_V \rho \widetilde{\boldsymbol{u_j}} \dot{\boldsymbol{u}}_{\boldsymbol{j}} dV = \\ &= -\langle \dot{\boldsymbol{\eta}}^T \widehat{\boldsymbol{h2}}_{\boldsymbol{j}} \boldsymbol{\eta} \rangle + \langle \boldsymbol{\eta}^T (\widehat{\boldsymbol{h1}}_{\boldsymbol{j}} + \widehat{\boldsymbol{h2}}_{\boldsymbol{j}} + \widehat{\boldsymbol{h4}}_{\boldsymbol{j}}) \dot{\boldsymbol{\eta}} \rangle + \widehat{\boldsymbol{h5}} \dot{\boldsymbol{\eta}} \end{aligned} \tag{17}$$

$$\begin{aligned}\dot{\mathbf{h}} &= \int_V \rho \widetilde{\boldsymbol{u_j}} \ddot{\boldsymbol{u}}_j dV = \\ &= \langle \dot{\boldsymbol{\eta}}^T (\widehat{\boldsymbol{h1}}_j + \widehat{\boldsymbol{h4}}_j) \dot{\boldsymbol{\eta}} \rangle - \langle \ddot{\boldsymbol{\eta}}^T \widehat{\boldsymbol{h2}}_j \boldsymbol{\eta} \rangle + \langle \boldsymbol{\eta}^T (\widehat{\boldsymbol{h1}}_j + \widehat{\boldsymbol{h2}}_j + \widehat{\boldsymbol{h4}}_j) \ddot{\boldsymbol{\eta}} \rangle + \widehat{\boldsymbol{h5}} \ddot{\boldsymbol{\eta}}\end{aligned} \tag{18}$$

The terms $\widehat{\boldsymbol{B}}_{\boldsymbol{jk}}$, $\widehat{\boldsymbol{C}}_{\boldsymbol{jk}}$, $\widehat{\boldsymbol{h1}}_j$, $\widehat{\boldsymbol{h2}}_j$, $\widehat{\boldsymbol{h4}}_j$ and $\widehat{\boldsymbol{h5}}$ are constant matrices presented in [1].

The final EOM for rigid-body DOF, applying the mean-axis constraints, are presented below:

$$m\dot{\boldsymbol{V}}_b - m\widetilde{\boldsymbol{s_{C,b}}}\dot{\boldsymbol{\omega}}_b = \boldsymbol{F}_b^{\boldsymbol{ext,nc}} + m\boldsymbol{g_b} - m\widetilde{\boldsymbol{\omega_b}}\boldsymbol{V_b} - m\widetilde{\boldsymbol{\omega_b}}^2\boldsymbol{s_{C,b}} \tag{19}$$

$$\begin{aligned}m\widetilde{\boldsymbol{s_{C,b}}}\dot{\boldsymbol{V}}_b + (\boldsymbol{J_{O,b}} + \Delta\boldsymbol{J_{O,b}})\dot{\boldsymbol{\omega}}_b = \boldsymbol{M}_{\boldsymbol{O,b}}^{\boldsymbol{ext,nc}} + m\widetilde{\boldsymbol{s_{C,b}}}\boldsymbol{g_b} \\ -m\widetilde{\boldsymbol{s_{C,b}}}\widetilde{\boldsymbol{\omega_b}}\boldsymbol{V_b} - \widetilde{\boldsymbol{\omega_b}}(\boldsymbol{J_{O,b}} + \Delta\boldsymbol{J_{O,b}})\boldsymbol{\omega_b} + \Delta\dot{\boldsymbol{J}}_{\boldsymbol{O,b}}\boldsymbol{\omega_b} + \dot{\mathbf{h}} + \widetilde{\boldsymbol{\omega_b}}\mathbf{h}\end{aligned} \tag{20}$$

### *2.1.2 Elastic DOF*

The equations of motion of the elastic DOF are obtained by solving the Lagrange equation:

$$\frac{d}{dt}\left(\frac{\partial \mathcal{L}}{\partial \dot{\boldsymbol{q}}_{\boldsymbol{k}}}\right) - \frac{\partial \mathcal{L}}{\partial \boldsymbol{q_k}} + \frac{\partial \mathcal{F}}{\partial \dot{\boldsymbol{q}}_{\boldsymbol{k}}} = \boldsymbol{Q_k} \tag{21}$$

The *Lagrangian* term in Equation 21 is $\mathcal{L} = \mathcal{T} - \mathcal{U}$, which is the difference between kinetic and potential energies.

The kintic energy of the flexible aircraft is given by:

$$\mathcal{T} = \frac{1}{2}\int_V \rho \left(\boldsymbol{V_b} + \dot{\boldsymbol{u}}_b + \widetilde{\boldsymbol{\omega_b}}\boldsymbol{s_b} + \widetilde{\boldsymbol{\omega_b}}\boldsymbol{u_b}\right)^T \left(\boldsymbol{V_b} + \dot{\boldsymbol{u}}_b + \widetilde{\boldsymbol{\omega_b}}\boldsymbol{s_b} + \widetilde{\boldsymbol{\omega_b}}\boldsymbol{u_b}\right) \tag{22}$$

The potential energy of the flexible aircraft can be divided into elastic strain energy and gravitational potential energy:

$$\begin{aligned}\mathcal{U} &= \mathcal{U}_{strain} + \mathcal{U}_{grav} = \\ &= \frac{1}{2}\boldsymbol{q}^T\mathbf{K}\boldsymbol{q} - m(\boldsymbol{R_{O,b}} + \boldsymbol{s_{C,b}} + \boldsymbol{u_{C,b}})^T\boldsymbol{g_b}\end{aligned} \tag{23}$$

Rayleigh's dissipation function can be expressed in terms of the damping matrix $\mathbf{C}$:

$$\mathcal{F} = \frac{1}{2}\dot{\boldsymbol{q}}^T\mathbf{C}\dot{\boldsymbol{q}} \tag{24}$$

Due to the orthogonality of each mode shape with respect to $\mathbf{M}$ and $\mathbf{K}$, the generalized modal mass and stiffness matrices can be defined. The generalized modal mass matrix is expressed as

$\boldsymbol{\mu} = {\boldsymbol{\Phi_m}}^T \mathbf{M} \boldsymbol{\Phi_m}$, while the generalized modal stiffness matrix is given by $\boldsymbol{\kappa} = {\boldsymbol{\Phi_m}}^T \mathbf{K} \boldsymbol{\Phi_m}$. Furthermore, it is assumed that the generalized modal force is $\boldsymbol{\varphi} = {\boldsymbol{\Phi_m}}^T \mathbf{Q}$ and the generalized modal damping matrix as $\boldsymbol{\beta} = {\boldsymbol{\Phi_m}}^T \mathbf{C} \boldsymbol{\Phi_m}$.

Solving the Lagrange's equation for modal coordinate $\boldsymbol{\eta}$, expanding only the terms related to displacement $\boldsymbol{u_b}$ and displacement rate $\boldsymbol{\dot{u}_b}$ in the kinetic energy equation, and excluding the generalized force due to the gravitational field by appling the practical mean-axis constraints, the EOM for the elastic DOF is given by:

$$\begin{aligned} \boldsymbol{\mu}\ddot{\boldsymbol{\eta}} + \left(\sum_{j=1}^{3} \widehat{\boldsymbol{h}}_j \boldsymbol{\eta} {\boldsymbol{e_j}}^T + \widehat{\boldsymbol{h5}}^T\right) \dot{\boldsymbol{\omega}}_b = \boldsymbol{\vartheta} - \boldsymbol{\kappa}\boldsymbol{\eta} - \boldsymbol{\beta}\dot{\boldsymbol{\eta}} - 2\sum_{j=1}^{3} \widehat{\boldsymbol{h}}_j \dot{\boldsymbol{\eta}} {\boldsymbol{e_j}}^T \boldsymbol{\omega_b} \\ -\tfrac{1}{2}\sum_{j=1}^{3}\sum_{k=1}^{3} \left( (\widehat{\boldsymbol{B}}_{\boldsymbol{jk}} + {\widehat{\boldsymbol{B}}_{\boldsymbol{jk}}}^T)\boldsymbol{\eta} + {\widehat{\boldsymbol{C}}_{\boldsymbol{jk}}}^T \right) {\boldsymbol{\omega_b}}^T \boldsymbol{e_j} {\boldsymbol{e_k}}^T \boldsymbol{\omega_b} \end{aligned} \tag{25}$$

Where $\boldsymbol{\mu}$, $\boldsymbol{\kappa}$ and $\boldsymbol{\varphi}$ are diagonal matrices.

### 2.2 Rigid Aircraft

The EOM for the rigid aircraft is obtained by setting the number of elastic modes to zero. Consequently, under this assumption, the matrix $\boldsymbol{\Phi_m}$ and the vector $\boldsymbol{\eta}$ are nullified, causing all terms in the elastic equation and some terms of the angular momentum equation to vanish. Therefore, the EOM for the rigid aircraft are given by:

$$m\dot{\boldsymbol{V}}_b - m\widetilde{\boldsymbol{s_{C,b}}}\dot{\boldsymbol{\omega}}_b = \boldsymbol{F_b^{ext,nc}} + m\boldsymbol{g_b} - m\widetilde{\boldsymbol{\omega_b}}\boldsymbol{V_b} - m\widetilde{\boldsymbol{\omega_b}}^2\boldsymbol{s_{C,b}} \tag{26}$$

$$m\widetilde{\boldsymbol{s_{C,b}}}\dot{\boldsymbol{V}}_b + \boldsymbol{J_{O,b}}\dot{\boldsymbol{\omega}}_b = \boldsymbol{M_{O,b}^{ext,nc}} + m\widetilde{\boldsymbol{s_{C,b}}}\boldsymbol{g_b} - m\widetilde{\boldsymbol{s_{C,b}}}\widetilde{\boldsymbol{\omega_b}}\boldsymbol{V_b} - \widetilde{\boldsymbol{\omega_b}}\boldsymbol{J_{O,b}}\boldsymbol{\omega_b} \tag{27}$$

## 3 EXTERNAL NON-CONSERVATIVE LOADS

The external non-conservative forces and moments are calculated by summing the aerodynamic and propulsive contributions, as presented in the following equation:

$$\begin{aligned} \boldsymbol{F_b^{ext,nc}} &= \boldsymbol{F_{aero,b}} + \boldsymbol{F_{prop,b}} \\ \boldsymbol{M_{O,b}^{ext,nc}} &= \boldsymbol{M_{aero,O,b}} + \boldsymbol{M_{prop,O,b}} \\ \boldsymbol{\vartheta} &= \boldsymbol{\vartheta_{aero}} + \boldsymbol{\vartheta_{prop}} \end{aligned} \tag{28}$$

Where $\boldsymbol{F_b^{ext,nc}}$ is the vector of external non-conservative forces, $\boldsymbol{M_{O,b}^{ext,nc}}$ is the vector of external non-conservative moments, and $\boldsymbol{\vartheta}$ is the vector of non-conservative generalized loads.

Quasi-steady models, fully developed in the ITA's course AB-276 [17], are employed for the computation of aerodynamic and propulsive loads.

### 3.1 Aerodynamic Model

The total aerodynamic forces and moments are considered as the sum of the contributions of lifting surfaces, fuselage and nacelles, as presented in the following equation:

$$\begin{aligned} \boldsymbol{F_{aero,b}} &= \boldsymbol{F_{VLM}} \\ \boldsymbol{M_{aero,O,b}} &= \boldsymbol{M_{VLM,O}} + \boldsymbol{M_{aero,fus}} + \boldsymbol{M_{aero,lnac}} + \boldsymbol{M_{aero,rnac}} \\ \boldsymbol{\vartheta_{aero}} &= \boldsymbol{\vartheta_{aero,VLM}} + \boldsymbol{\vartheta_{aero,fus}} + \boldsymbol{\vartheta_{aero,lnac}} + \boldsymbol{\vartheta_{aero,rnac}} \end{aligned} \tag{29}$$

The quasi-steady aerodynamics of the lifting surfaces are modeled using Hedman's VLM [15], using the Prandtl-Glauert rule is used to account for compressible effects.

The VLM yields the matrix of aerodynamic influence coefficient (**AIC**) that relates the pressure coefficient ($\Delta C_p$) at each panel with the dimensionless normalwashes, that are the normal velocities at each panel's control point ($\Delta C_p = A\overline{w}$). The control surface deflection affects the normal direction of the panels, which modifies $\overline{w}$. The total aerodynamic force is obtained through the following equation:

$$\boldsymbol{F_{VLM}} = \sum_{j=1}^{n_p} \left( \widehat{\boldsymbol{u}}_{\boldsymbol{F,j}} \overline{q}_j S_j \Delta C_{p,j} \right) \tag{30}$$

where $n_p$ is the number of panels, $\widehat{\boldsymbol{u}}_{\boldsymbol{F,j}}$ is the direction of the flow velocity on the $j$th panel, $\overline{q}_j$ is the dynamic pressure of the $j$th panel, $S_j$ is the area of the $j$th panel and $\Delta C_{p,j}$ is the pressure coefficient of the $j$th panel.

The flexibility of the aircraft has two effects on the quasi-steady VLM forces:

- The local velocities due to bending and twisting will affect $\widehat{\boldsymbol{u}}_{\boldsymbol{F,j}}$ and $\overline{q}_j$;
- The quasi-static effect of twisting on the local incidence, modifying $\widehat{\boldsymbol{u}}_{\boldsymbol{F,j}}$.

The total VLM aerodynamic moment about $O$ is given by:

$$\boldsymbol{M_{VLM,O}} = \sum_{j=1}^{n_p} \left[ \boldsymbol{R_{C,j}} \times \left( \widehat{\boldsymbol{u}}_{\boldsymbol{F,j}} \overline{q}_j S_{ref} \Delta C_{p,j} \right) \right] \tag{31}$$

where $\boldsymbol{R_{C,j}}$ is the position vector of the $j$th control point in relation to the origin of the body system $O$.

The total VLM aerodynamic generalized modal forces are calculated with the following equation:

$$\boldsymbol{\vartheta_{aero,VLM}} = \boldsymbol{\varphi_{C_p}} \text{diag}(\overline{q}) \Delta C_p + \boldsymbol{\varphi_{C_d}} \text{diag}(\overline{q}) \left( C_{d,0} + C_{d,ind} \right) \tag{32}$$

where the matrices $\boldsymbol{\varphi_{C_p}}$ and $\boldsymbol{\varphi_{C_d}}$ are the sum of the elastic displacements of the $j$th panel aerodynamic center in the directions normal and tangential to the panel, respectively. These matrices are calculated before the simulations to increase the computational efficiency.

The fuselage lift and side forces are neglected, since they are usually small when compared with those from the wing and tails. Therefore, the relevant fuselage aerodynamic loads are given by the pitching and yawing moments. The same is valid for both engines nacelles.

The fuselage and nacelles aerodynamic moments ($\boldsymbol{M_{aero,fus}}$, $\boldsymbol{M_{aero,lnac}}$, $\boldsymbol{M_{aero,rnac}}$, $\boldsymbol{\vartheta_{aero,fus}}$, $\boldsymbol{\vartheta_{aero,lnac}}$ and $\boldsymbol{\vartheta_{aero,rnac}}$) are estimated using the methodologies presented in [21], and are caused by the *Munk effect*.

### 3.2 Propulsive Model

The propulsive model employed in this work is quasi-steady, therefore the current value of thrust does not depend on past states or inputs. Additionally, the direction of the thrust modifies according to structural deformation. However, the gyroscopic effects generated by the rotating engine parts are not considered.

The propulsive model was developed in the ITA's course AB-276, and the methodologies are detailed in the course's material [17].

The thrust of each engine is assumed directly proportional to throttle position, and is calculated with the following equation:

$$T = \delta_t T_{max,ref} \left( \frac{\rho}{\rho_{ref}} \right)^{n_\rho} \tag{33}$$

Where the maximum thrust $T_{max,ref}$ is assumed equal to 100000 N and the factor $n_\rho$ equal to 0.8 for all flight conditions.

The propulsive loads at the origin of the body axes, acting on the flexible aircraft, are calculated with the following expressions:

$$\begin{array}{c} \boldsymbol{F_{prop,b}} = \sum_{e=1}^{n_e} \left( \boldsymbol{I_3} + \widetilde{\boldsymbol{\varphi_{K_e,b}}} \right) \boldsymbol{C_{b/P_e}} \boldsymbol{e_1} T_e \\ \boldsymbol{M_{prop,O,b}} = \sum_{e=1}^{n_e} \text{skew} \left( \boldsymbol{s_{K_e,b}} + \boldsymbol{s_{K_eP_e,b}} + \boldsymbol{u_{P_e,b}} \right) \left( \boldsymbol{I_3} + \widetilde{\boldsymbol{\varphi_{K_e,b}}} \right) \boldsymbol{C_{b/P_e}} \boldsymbol{e_1} T_e \\ \boldsymbol{\vartheta_{prop}} = \sum_{e=1}^{n_e} \left( \Phi_{K_e,t} - \widetilde{\boldsymbol{s_{K_eP_e,b}}} \boldsymbol{\Phi_{K_e,r}} \right)^T \left( \boldsymbol{I_3} + \widetilde{\boldsymbol{\varphi_{K_e,b}}} \right) \boldsymbol{C_{b/P_e}} \boldsymbol{e_1} T_e \end{array} \tag{34}$$

Where:

- $P_e$ is the point of action of the $e$th engine thrust;
- $K_e$ is the point of the engine pylon beam that is rigidly connected with $P_e$;
- $n_e$ is the number of engines;
- $\boldsymbol{\varphi_{K_e,b}}$ is the vector of rotational displacements of the point $K_e$;
- $C_{b/P_e}$ is the transformation matrix from the propulsive system of the $e$th engine to the body system in the undeformed aircraft;
- $\boldsymbol{s_{K_e,b}}$ is the undeformed position vector of $K_e$ with respect to $O$;
- $\boldsymbol{s_{K_eP_e,b}}$ is the undeformed position vector from $K_e$ to $P_e$;
- $\boldsymbol{u_{P_e,b}}$ is the elastic displacement of $P_e$;
- $\Phi_{K_e,t}$ and $\Phi_{K_e,r}$ are the translational and rotational DOF of the mode shapes of the grid point $K_e$, respectively.

The transformation matrix $\boldsymbol{C_{b/P_e}} = \left( \boldsymbol{C_2}(\iota_{P_e}) \boldsymbol{C_3}(\tau_{P_e}) \right)^T$, where:

$$\boldsymbol{C_2}(\iota_{P_e}) = \begin{bmatrix} \cos \iota_{P_e} & 0 & -\sin \iota_{P_e} \\ 0 & 1 & 0 \\ \sin \iota_{P_e} & 0 & \cos \iota_{P_e} \end{bmatrix} \tag{35}$$

$$\boldsymbol{C_3}(\tau_{P_e}) = \begin{bmatrix} \cos \tau_{P_e} & \sin \tau_{P_e} & 0 \\ -\sin \tau_{P_e} & \cos \tau_{P_e} & 0 \\ 0 & 0 & 1 \end{bmatrix} \tag{36}$$

## 4 STRUCTURAL DYNAMICS MODEL

The structural dynamics model is developed using finite element method (FEM). The necessary inputs for constructing this model comprise the inertial and geometric properties, alongside the bending and torsional rigidity of the airplane's primary structures, as detailed in the materials provided within ITA's AB-276 course [17]. Notably, these properties exhibit slight discrepancies from those documented in [6], resulting in differences up to 12% in the modal frequency when considering the modes with frequency below 20Hz. The output that this model generates for the flight dynamics and loads analysis is the mass, stiffness and damping matrices ($\mathbf{M}$, $\mathbf{K}$ and $\mathbf{C}$). The MSC Nastran bulk data entries [22] were employed do build the model.

A summary of the structural model main entries defined within the Nastran card is provided in Table 1.

Table 1: Summary of structural model entries

| Entry name | Number of entries |
|---|---|
| CBEAM | 50 |
| CONM2 | 342 |
| GRID | 393 |
| PBEAM | 31 |
| RBE2 | 27 |

A viscous damping formulation is employed to incorporate the damping effect within the structural dynamic model. This formulation is described in [20].

The generalized damping matrix $\boldsymbol{\beta}$ takes the form of a diagonal matrix and its computation relies on the modal damping coefficient $\xi_i$ of a number of natural modes. Each element of the diagonal matrix is calculated according to the following expression:

$$[\boldsymbol{\beta_{ii}}] = 2\xi_i \left[\omega_{n_i}\right] [\boldsymbol{\mu_{ii}}] \tag{37}$$

Where the index $i$ indicates the $i$-th natural mode and the modal damping $\xi_i$ is assumed equal to 0.02 for all natural modes.

The mass configuration selected for all the analysis is the design-point cruise weight (DW) presented in reference [6]. However, it is essential to acknowledge that the structural model developed for this study is reliant on the weight and structural parameters drawn from the materials of ITA's AB-276 course [17]. Consequently, minor disparities exist between the DW mass configurations employed in this present analysis and the DW configuration defined in [6]. A summary of these differences is provided in Table 2.

## 5 INTERNAL LOADS RECOVERY

The force summation method (FSM) is adopted for internal load calculations. The preference for FSM over alternative methods such as mode displacement method (MDM) or mode acceleration method (MAM) stems from its capability to compute individual load components and its superior convergence characteristics.

Table 2: Comparison of DW mass configuration

| Property | Unit | Present Work | Reference [6] | Difference |
|---|---|---|---|---|
| $m$ | $[kg]$ | 55764 | 55788 | $-0.04\%$ |
| $x_{CG}$ | $[m]$ | 18.301 | 18.308 | $-0.04\%$ |
| $y_{CG}$ | $[m]$ | 0.011 | 0.011 | $0.00\%$ |
| $z_{CG}$ | $[m]$ | $-0.556$ | $-0.540$ | $4.81\%$ |
| $I_{xx,CG}$ | $[kg.m^2]$ | $8.369 \times 10^5$ | $8.215 \times 10^5$ | $1.87\%$ |
| $I_{yy,CG}$ | $[kg.m^2]$ | $3.492 \times 10^6$ | $3.344 \times 10^6$ | $4.43\%$ |
| $I_{zz,CG}$ | $[kg.m^2]$ | $4.184 \times 10^6$ | $4.057 \times 10^6$ | $3.13\%$ |

For horizontal lifting surfaces, the notations are SLZ for shear force, BMX for bending moment and TMY for torsion moment. The reference axis for torsion moment calculation is the elastic axis. All the grid points (structural nodes) are positioned along the elastic axis.

The reference system employed in the loads analysis differs from the body axes utilized in flight dynamics analysis. The loads reference system is presented in Figure 3.

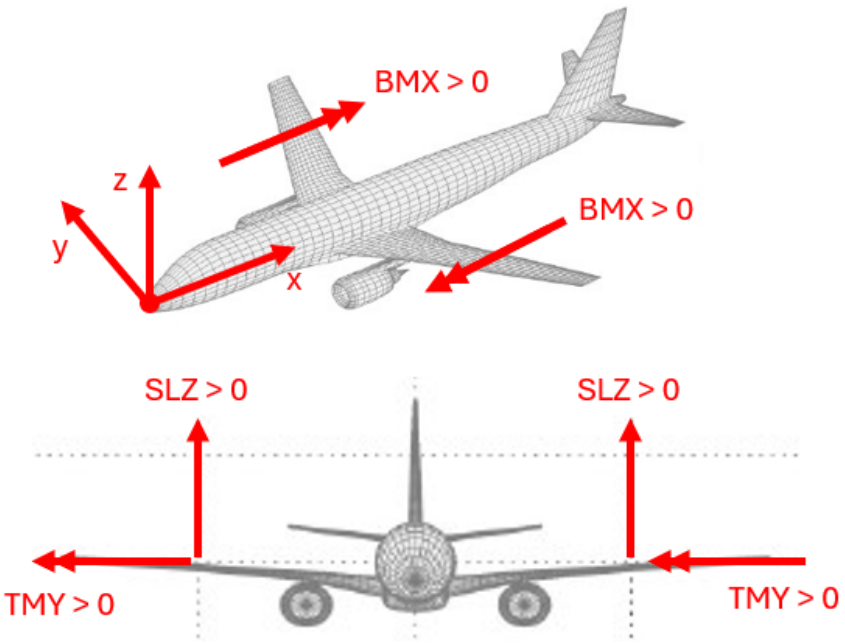


Figure 3: Structural loads reference system

To construct the internal loads diagrams, the lifting surfaces undergo segmentation into stations. The border of each station is the grid points of the FEM model. The half wing has 14 nodes and 13 stations, the half horizontal tail has 6 nodes and 5 stations, and the vertical tail has 7 nodes and 6 stations. Figure 4 visually depicts the stations along the left wing.

The nodal load is considered as the resultant forces and moments exerted at the station immediately subsequent to the node, spanning from the root to the tip of the lifting surface. For example, the nodal loads at Node 1, depicted in Figure 4, is the resultant load of Station 1.

To calculate the nodal loads, that is the total forces and moments at each station, the FSM is employed. The load equations for a flexible aircraft with inertially coupled EOM are derived in [1] through the application of the principle of momentum, commonly referred to as the Newton-

Euler method. The equations of Newton-Euler are expressed as follows:

$$\frac{d}{dt}\begin{bmatrix} \boldsymbol{H}_{t,j} \\ \boldsymbol{H}_{r,j} \end{bmatrix} = \begin{bmatrix} \boldsymbol{F}_j \\ \boldsymbol{M}_j \end{bmatrix} = \begin{bmatrix} m_j \ddot{\boldsymbol{R}}_j \\ \boldsymbol{J}_j \left(\dot{\boldsymbol{\omega}}_b + \ddot{\boldsymbol{\varphi}}_i\right) + \widetilde{\boldsymbol{\omega}_b} \boldsymbol{J}_j \left(\boldsymbol{\omega}_b + \dot{\boldsymbol{\varphi}}_i\right) \end{bmatrix} \tag{38}$$

Where $\boldsymbol{H}_{t,j}$ and $\boldsymbol{H}_{r,j}$ are the translational and rotational momentum vector, respectively, and $\boldsymbol{F}_j$ and $\boldsymbol{M}_j$ denotes the total forces and moments applied at the mass element $j$.

The resulting force and moment at the grid point $i$ is determined based on the contributions of the elastic forces ($\boldsymbol{F}_i^{el}$ and $\boldsymbol{M}_i^{el}$), gravity forces ($\boldsymbol{G}_j$) and external non-conservative forces and moments ($\boldsymbol{F}_i^{ext,nc}$ and $\boldsymbol{M}_i^{ext,nc}$), as presented in the expression below:

$$\begin{bmatrix} \boldsymbol{F}_i \\ \boldsymbol{M}_i \end{bmatrix} = \begin{bmatrix} \boldsymbol{F}_i^{ext,nc} \\ \boldsymbol{M}_i^{ext,nc} \end{bmatrix} + \begin{bmatrix} \boldsymbol{F}_i^{el} \\ \boldsymbol{M}_i^{el} \end{bmatrix} + \begin{bmatrix} \boldsymbol{0} \\ -\widetilde{\boldsymbol{d}_j}(\boldsymbol{F}_i^{ext,nc} + \boldsymbol{F}_i^{el}) \end{bmatrix} + \begin{bmatrix} \boldsymbol{G}_j \\ \boldsymbol{0} \end{bmatrix} \tag{39}$$

The forces exerted on a grid point $i$ and a mass element $j$ are depicted in Figure 5.

Further expanding the Newton-Euler equation, and substituting the gravitational force $\boldsymbol{G}_j = m_j \boldsymbol{g}_b$, yields:

$$\begin{aligned} \begin{bmatrix} m_j \ddot{\boldsymbol{R}}_j \\ m_j \widetilde{\boldsymbol{d}_j} \ddot{\boldsymbol{R}}_j + \boldsymbol{J}_j \left(\dot{\boldsymbol{\omega}}_b + \ddot{\boldsymbol{\varphi}}_i\right) + \widetilde{\boldsymbol{\omega}_b} \boldsymbol{J}_j \left(\boldsymbol{\omega}_b + \dot{\boldsymbol{\varphi}}_i\right) \end{bmatrix} &= \begin{bmatrix} \boldsymbol{F}_i^{ext,nc} \\ \boldsymbol{M}_i^{ext,nc} \end{bmatrix} + \begin{bmatrix} \boldsymbol{F}_i^{el} \\ \boldsymbol{M}_i^{el} \end{bmatrix} \\ &+ \begin{bmatrix} m_j \boldsymbol{I_3} & \boldsymbol{0} \\ m_j \widetilde{\boldsymbol{d}_j} & \boldsymbol{I_3} \end{bmatrix} \begin{bmatrix} \boldsymbol{g}_b \\ \boldsymbol{0} \end{bmatrix} \end{aligned} \tag{40}$$

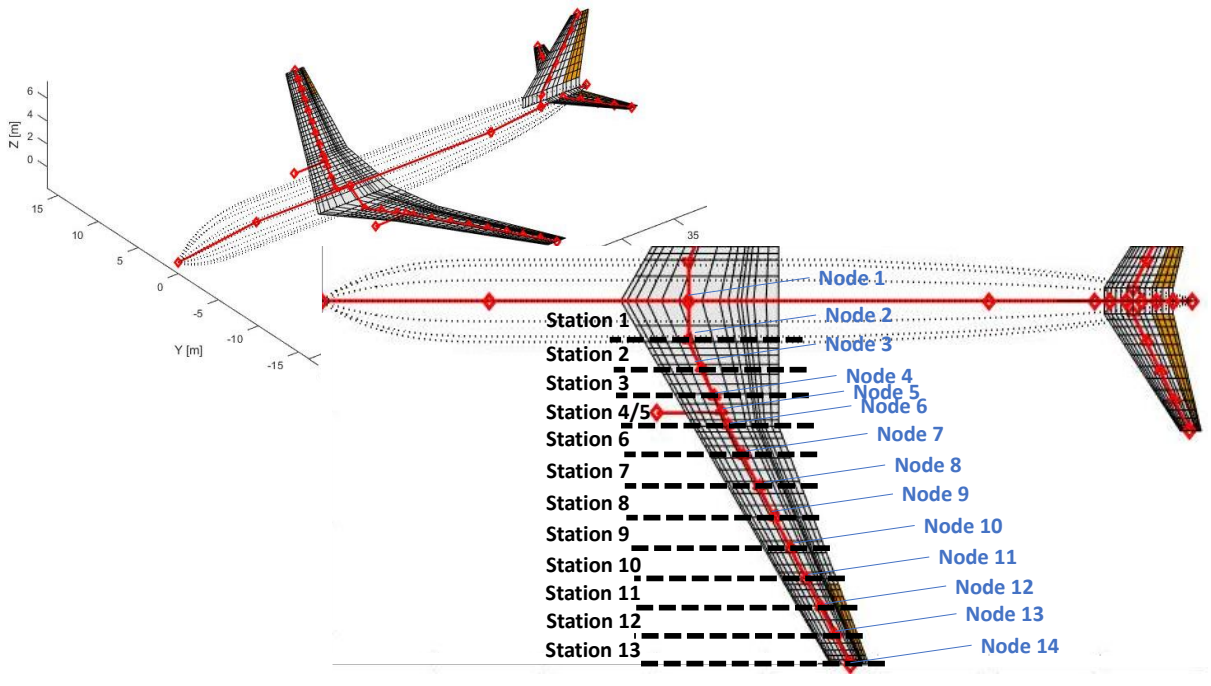


Figure 4: Loads stations of left wing

In the FSM, the nodal loads are elastic forces obtained by the summation of forces. Therefore, the nodal loads exerted on the grid point $i$ is obtained by the following equation:

$$\boldsymbol{L_i} = -\begin{bmatrix} \boldsymbol{F_i^{el}} \\ \boldsymbol{M_i^{el}} \end{bmatrix} = \begin{bmatrix} \boldsymbol{F_i^{ext,nc}} \\ \boldsymbol{M_i^{ext,nc}} \end{bmatrix} - \begin{bmatrix} m_j \boldsymbol{I_3} & \boldsymbol{0} \\ m_j \widetilde{\boldsymbol{d_j}} & \boldsymbol{J_j} \end{bmatrix} \begin{bmatrix} \ddot{\boldsymbol{R}}_j - \boldsymbol{g_b} \\ \dot{\boldsymbol{\omega}}_b + \ddot{\boldsymbol{\varphi}}_i \end{bmatrix} - \begin{bmatrix} \boldsymbol{0} \\ \widetilde{\boldsymbol{\omega}_b} \boldsymbol{J_j} \end{bmatrix} (\boldsymbol{\omega_b} + \dot{\boldsymbol{\varphi}}_i) \tag{41}$$

The first term on the right-hand side of Equation 41 represents the external non-conservative forces and moments, presented in Section 3, while all other terms are associated to inertial loads.

The model of the GNBA (*generic narrow-body airliner*) employed in the analysis may feature $n$ lumped masses rigidly connected to a single grid point $i$. Consequently, each grid point may have the contribution of $n_m$ mass elements to calculate the inertial loads.

To calculate the inertial contribution of Equation 41, the translational inertial acceleration of the mass element is obtained through the following equation:

$$\begin{aligned} \ddot{\boldsymbol{R}}_j =& \dot{\boldsymbol{V}}_b + \widetilde{\boldsymbol{\omega}_b} \boldsymbol{V_b} + \left( \widetilde{\boldsymbol{\omega}_b}^2 + \widetilde{\dot{\boldsymbol{\omega}}_b} \right) \boldsymbol{s_j} \\ &+ \ddot{\boldsymbol{u}}_j + 2\widetilde{\boldsymbol{\omega}_b} \dot{\boldsymbol{u}}_j + \left( \widetilde{\boldsymbol{\omega}_b}^2 + \widetilde{\dot{\boldsymbol{\omega}}_b} \right) \boldsymbol{u_j} \end{aligned} \tag{42}$$

Where in the right-hand side of the first line is described the rigid body contribution and in the second line is presented the elastic contribution.

The elastic displacement, velocities and accelerations are expressed using the modal approach as the following:

$$\begin{aligned} \boldsymbol{u_j} &= \begin{bmatrix} \boldsymbol{I_3} & , & -\widetilde{\boldsymbol{s_j}} \end{bmatrix} \boldsymbol{\Phi_i} \boldsymbol{\eta} \\ \dot{\boldsymbol{u}}_j &= \begin{bmatrix} \boldsymbol{I_3} & , & -\widetilde{\boldsymbol{s_j}} \end{bmatrix} \boldsymbol{\Phi_i} \dot{\boldsymbol{\eta}} \\ \ddot{\boldsymbol{u}}_j &= \begin{bmatrix} \boldsymbol{I_3} & , & -\widetilde{\boldsymbol{s_j}} \end{bmatrix} \boldsymbol{\Phi_i} \ddot{\boldsymbol{\eta}} \end{aligned} \tag{43}$$

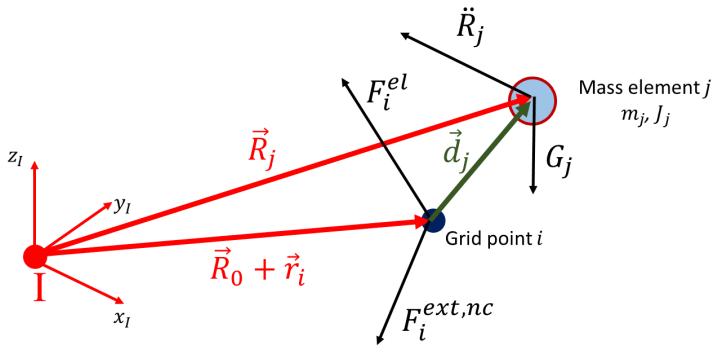


Figure 5: Forces at grid point $i$ and lumped mass $j$

Isolating solely the inertial contribution terms from Equation 41 and substituting Equations 42 and 43 into Equation 41, yields the inertial contribution loads for a mass element $j$:

$$\begin{aligned}\boldsymbol{L_j^{inertial}} = &- \boldsymbol{M_{gR_j}}\Bigg(\begin{bmatrix} \dot{\boldsymbol{V}}_{\boldsymbol{b}} + \widetilde{\boldsymbol{\omega}_{\boldsymbol{b}}}\boldsymbol{V_b} - \boldsymbol{g_b} \\ \dot{\boldsymbol{\omega}}_{\boldsymbol{b}} \end{bmatrix} + \begin{bmatrix} \widetilde{\boldsymbol{\omega}_{\boldsymbol{b}}}^2\boldsymbol{s_j} \\ \boldsymbol{0} \end{bmatrix} \\ &+ \begin{bmatrix} 2\widetilde{\boldsymbol{\omega}_{\boldsymbol{b}}} \\ \boldsymbol{0} \end{bmatrix} \begin{bmatrix} \boldsymbol{I_3} & -\widetilde{\boldsymbol{d_j}} \end{bmatrix} \boldsymbol{\Phi_i}\dot{\boldsymbol{\eta}} + \begin{bmatrix} \widetilde{\boldsymbol{\omega}_{\boldsymbol{b}}}^2 + \widetilde{\dot{\boldsymbol{\omega}}_{\boldsymbol{b}}} \\ \boldsymbol{0} \end{bmatrix} \begin{bmatrix} \boldsymbol{I_3} & -\widetilde{\boldsymbol{d_j}} \end{bmatrix} \boldsymbol{\Phi_i}\boldsymbol{\eta}\Bigg) \\ &- \begin{bmatrix} \boldsymbol{0} \\ \widetilde{\boldsymbol{\omega}_{\boldsymbol{b}}}\boldsymbol{J_j} \end{bmatrix} (\boldsymbol{\omega_b} + \boldsymbol{\Phi_{j,r}}\dot{\boldsymbol{\eta}}) - \boldsymbol{M_{gE_j}}\boldsymbol{\Phi_i}\ddot{\boldsymbol{\eta}}\end{aligned} \tag{44}$$

Where:

$$\boldsymbol{M_{gR_j}} = \begin{bmatrix} m_j\boldsymbol{I_3} & -m_j\widetilde{\boldsymbol{s_j}} \\ m_j\widetilde{\boldsymbol{d_j}} & \boldsymbol{J_{g,j}} - m_j\widetilde{\boldsymbol{d_j}}\widetilde{\boldsymbol{r_i}} \end{bmatrix} \tag{45}$$

$$\boldsymbol{M_{gE_j}} = \begin{bmatrix} m_j\boldsymbol{I_3} & -m_j\widetilde{\boldsymbol{d_j}} \\ m_j\widetilde{\boldsymbol{d_j}} & \boldsymbol{J_{g,j}} \end{bmatrix} \tag{46}$$

$$\boldsymbol{J_{g,j}} = \boldsymbol{J_j} + \widetilde{\boldsymbol{d_j}}^T\widetilde{\boldsymbol{d_j}}m_j \tag{47}$$

The nodal and internal loads are computed by summing the external non-conservative and inertial contributions. To calculate the relevant nodal loads for a horizontal lifting surface (vertical force FZ and torsion moment MY) at station $i$, the following equations are employed:

$$FZ_i = \sum_i L_{j,FZ}^{inertial} + \sum_i F_{aero,k,z} + \sum_i F_{prop,e,z} \tag{48}$$

$$\begin{aligned}MY_i = &\sum_i L_{j,MY}^{inertial} + \sum_i \left(\widetilde{\boldsymbol{d_k}}\boldsymbol{F_{aero,k}}\right)_y \\ &+ \sum_i \left[\left(\widetilde{\boldsymbol{d_e}}\boldsymbol{F_{prop,e}}\right)_y + M_{prop,Pe,e,y}\right]\end{aligned} \tag{49}$$

Where $\boldsymbol{d_k}$ and $\boldsymbol{d_e}$ are the position vector of the k-*th* aerodynamic panel and e-*th* engine point, respectively, in relation to the station $i$ node.

To calculate the relevant internal loads for a horizontal lifting surface (SLZ, BMX and TMY) at station $i$, the following equations are employed. It is essential to note that the integration must be conducted in an ordered manner from the surface tip to the root.

$$SLZ_i = SLZ_{i+1} + FZ_i \tag{50}$$

$$\begin{aligned} BMX_i =& BMX_{i+1} + \sum_i L^{inertial}_{j,MX} + \sum_i \left(\widetilde{\boldsymbol{d_k}}\boldsymbol{F_{aero,k}}\right)_x \\ &+ \sum_i \left[\left(\widetilde{\boldsymbol{d_e}}\boldsymbol{F_{prop,e}}\right)_x + M_{prop,Pe,e_x}\right] + d_{y,i}SLZ_{i+1} \end{aligned} \tag{51}$$

$$TMY_i = TMY_{i+1} + MY_i \tag{52}$$

The term $L^{inertial}_{j,FZ}$ corresponds to the inertial force FZ at mass element $j$, denoted by the third row of the vector $\boldsymbol{L^{inertial}_{j,}}$. Similarly, $L^{inertial}_{j,MX}$ and $L^{inertial}_{j,MY}$ represent the inertial moments MX and MY at grid point $i$ due to mass element $j$. The subscripts $x$, $y$ and $z$ designate the direction of the force or moment within that vector. The symbols $\sum_i$ indicate the summation of all element masses, aerodynamic panels, and engine loads across station $i$.

To calculate the nodal and internal loads for the rigid-body formulation, the same methodology outlined in the previous section is employed. However, in this case, it is assumed that the number of elastic modes is zero, resulting in the elimination of all terms related to elastic contribution to inertial loads. The Equation 44 may be rewritten for the rigid-body formulation as follows:

$$\boldsymbol{L^{inertial}_j} = -\boldsymbol{M_{gR_j}}\left(\begin{bmatrix} \dot{\boldsymbol{V}}_{\boldsymbol{b}} + \widetilde{\boldsymbol{\omega}_{\boldsymbol{b}}}\boldsymbol{V_b} - \boldsymbol{g_b} \\ \dot{\boldsymbol{\omega}}_{\boldsymbol{b}} \end{bmatrix} + \begin{bmatrix} \widetilde{\boldsymbol{\omega}_{\boldsymbol{b}}}^2\boldsymbol{s_j} \\ \boldsymbol{0} \end{bmatrix}\right) - \begin{bmatrix} \boldsymbol{0} \\ \widetilde{\boldsymbol{\omega}_{\boldsymbol{b}}}\boldsymbol{J_j} \end{bmatrix}\boldsymbol{\omega_b} \tag{53}$$

## 6 SIMULATION AND RESULTS

The equations of motion (Chapter 2), the aerodynamic and propulsive models (Chapter 3), the structural dynamics model (Chapter 4), and the equations for loads recovery (Chapter 5) are integrated within a dedicated simulation environment named FRAL (Flexible and Rigid Aircraft Loads). The FRAL was developed in MATLAB and is suitable for easy implementation of new functions.

The GNBA, developed in [6] is the platform employed in this work to calculate the flight maneuver loads. It is a conventional aircraft, with under-wing-mounted engines, conventional tail planes and seating capacity for 130 passengers, five-abreast. The MTOW is 64200 kgf. The main geometric parameters of GNBA are summarized in Table 3.

The trimmed flight condition corresponds to the initial conditions applied to all flight maneuver simulations, and it is assumed as a steady nonturnig flight (straight flight), with airspeed equal to VA (defined as 280 KEAS) and sea level altitude ($h = 0$).

The most relevant flight parameters and states, and also the control variables obtained for the trim condition of both flexible and rigid-body formulations are presented in Table 4.

A convergence analysis is made in order to define the number of normal modes. A satisfactory convergence of the flight loads is obtained with maximum $\omega_n$ equal to 25Hz. Therefore, this value will be employed at all the flight maneuvers simulated with the flexible aircraft formulation.

Table 3: The principal geometric parameter of the GNBA [6]

| Variable | Description | Unit | Value |
|---|---|---|---|
| $S_{ref}$ | Reference or equivalent wing planform area | $[m^2]$ | 116.0 |
| $AR$ | Equivalent wing aspect ratio | $[-]$ | 9.25 |
| $\lambda$ | Equivalent wing taper ratio | $[-]$ | 0.315 |
| $b_w$ | Equivalent wing span | $[m]$ | 32.756 |
| $c_w$ | Wing mean aerodynamic chord (MAC) | $[m]$ | 3.862 |
| $\Lambda_0$ | Wing leading edge sweepback angle | $[^\circ]$ | 30.00 |
| $\Lambda_{1/4}$ | Equivalent wing quarter-chord sweepback angle | $[^\circ]$ | 27.52 |
| $S_h$ | Horizontal tail planform area | $[m^2]$ | 25.03 |
| $AR_h$ | Horizontal tail aspect ratio | $[-]$ | 5.5 |
| $S_v$ | Vertical tail planform area | $[m^2]$ | 20.49 |
| $AR_v$ | Vertical tail aspect ratio (root to tip) | $[-]$ | 1.7 |
| $L_f$ | Fuselage length | $[m]$ | 39.15 |

The following maneuvers derived from subpart C of CS-25 specifications [19] are simulated in this work:

- Unchecked maneuver, simulated according to CS-25 §25.331(c)(1). It is presented at Section 6.1;
- Checked maneuver, simulated according to CS-25 §25.331(c)(2). It is presented at Section 6.2;
- Roll maneuver, simulated according to CS-25 §25.349(a). It is presented at Section 6.3;

Two simplifications are assumed in the simulation of the described flight maneuvers: a pilot model and the actuators dynamics are not implemented.

### 6.1 Unchecked Maneuver

The unchecked maneuver is simulated according to CS-25 §25.331(c)(1). Both elevators are deflected from 0 to the control stop with a fixed rate of -60°$/s$. The elevator control stop is assumed equal to $\pm 20^\circ$. The ramp of elevator deflection starts at the first time step of the simulation. Once the control stop is reached, the maximum deflection is sustained until the simulation's conclusion.

The unchecked maneuver simulation stops at the first time step following the attainment of the maximum limit load factor ($N_Z$), assumed equal to $2.5$. Figure 6 presents the time histories of the unchecked maneuver control variables and the response of translational (presented as load factor) and rotational accelerations.

The time history of wing, horizontal and vertical tails aerodynamic and total forces are presented in Figure 7. For wing and horizontal tail, the vertical resultant in the loads reference system (Figure 3) are presented, while for the vertical tail, the lateral resultant is plotted. The aerodynamic force is the summation of the contributions of all the surface panels aerodynamic forces, and the total force is the resultant of all forces acting on the surface (aerodynamic, inertial and propulsive contributions).

For the upcoming plots, two specific instants are selected: the initial condition at t = 0 and the moments when the wing experiences its maximum positive aerodynamic vertical force

Table 4: Comparison of flexible and rigid-body trim conditions

| Variable | Unit | Flexible | Rigid-body |
|---|---|---|---|
| $V$ | $[m/s]$ | 144.04 | 144.04 |
| $u$ | $[m/s]$ | 143.995 | 144.031 |
| $v$ | $[m/s]$ | 0.000 | 0.000 |
| $w$ | $[m/s]$ | 3.772 | 1.931 |
| $\alpha$ | $[^\circ]$ | 1.5006 | 0.7682 |
| $q$ | $[^\circ/s]$ | 0.0000 | 0.0000 |
| $\theta$ | $[^\circ]$ | 1.5006 | 0.7682 |
| $\beta$ | $[^\circ]$ | 0.0000 | 0.0000 |
| $\phi$ | $[^\circ]$ | $-0.0004$ | 0.0011 |
| $p$ | $[^\circ/s]$ | 0.0000 | 0.0000 |
| $r$ | $[^\circ/s]$ | 0.0000 | 0.0000 |
| $\psi$ | $[^\circ]$ | 0.0000 | 0.0000 |
| $\delta_{t_l}$ | $[\%]$ | 17.37 | 17.17 |
| $\delta_{t_r}$ | $[\%]$ | 17.37 | 17.17 |
| $i_t$ | $[^\circ]$ | $-1.0930$ | $-0.5766$ |
| $\delta_{e_l}$ | $[^\circ]$ | 0.0000 | 0.0000 |
| $\delta_{e_r}$ | $[^\circ]$ | 0.0000 | 0.0000 |
| $\delta_{a_l}$ | $[^\circ]$ | 0.0796 | $-0.0774$ |
| $\delta_{a_r}$ | $[^\circ]$ | $-0.0796$ | 0.0774 |
| $\delta_r$ | $[^\circ]$ | 0.0241 | 0.0008 |

($FZW_{aer,max}$), and the horizontal tail encounters its maximum negative aerodynamic vertical force ($FZHT_{aer,min}$).

The wing internal loads diagrams are presented in Figure 8. In order to better understand the wing internal loads diagrams, additional plots are presented.

Figure 9 presents two plots. The plots on the left side depict the vertical displacements of the wing's elastic axis and its rotation about the lateral axis, which is characterized as torsion. These

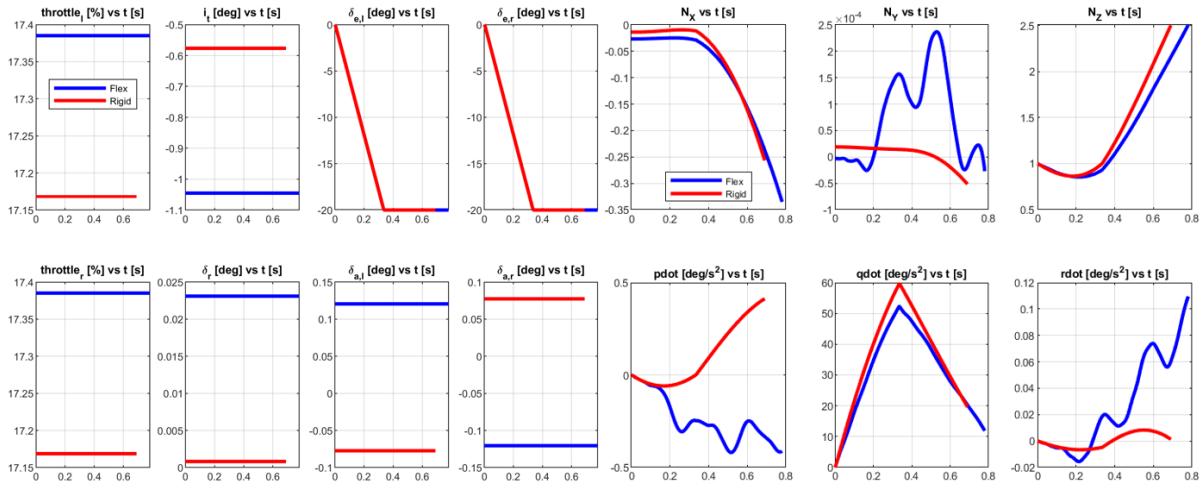


Figure 6: Time history of control variables and accelerations for unchecked maneuver simulation

values are calculated for the flexible aircraft formulation.

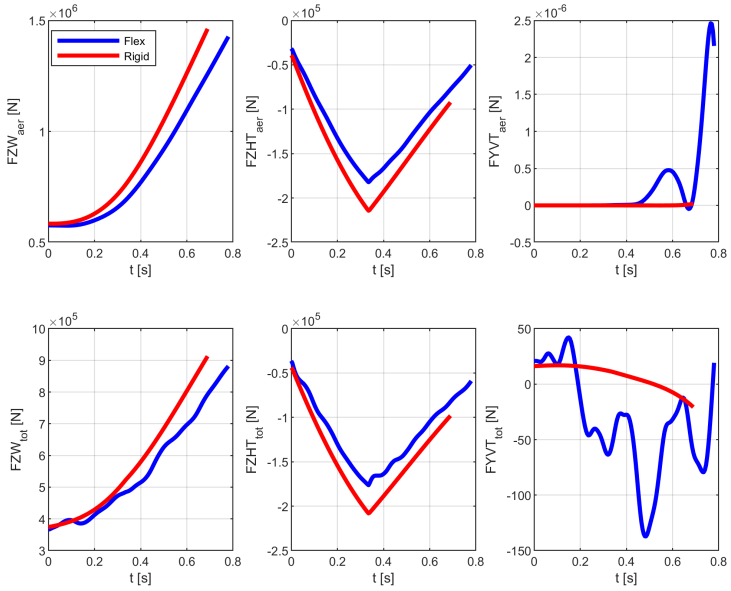


Figure 7: Time history of component forces for unchecked maneuver simulation

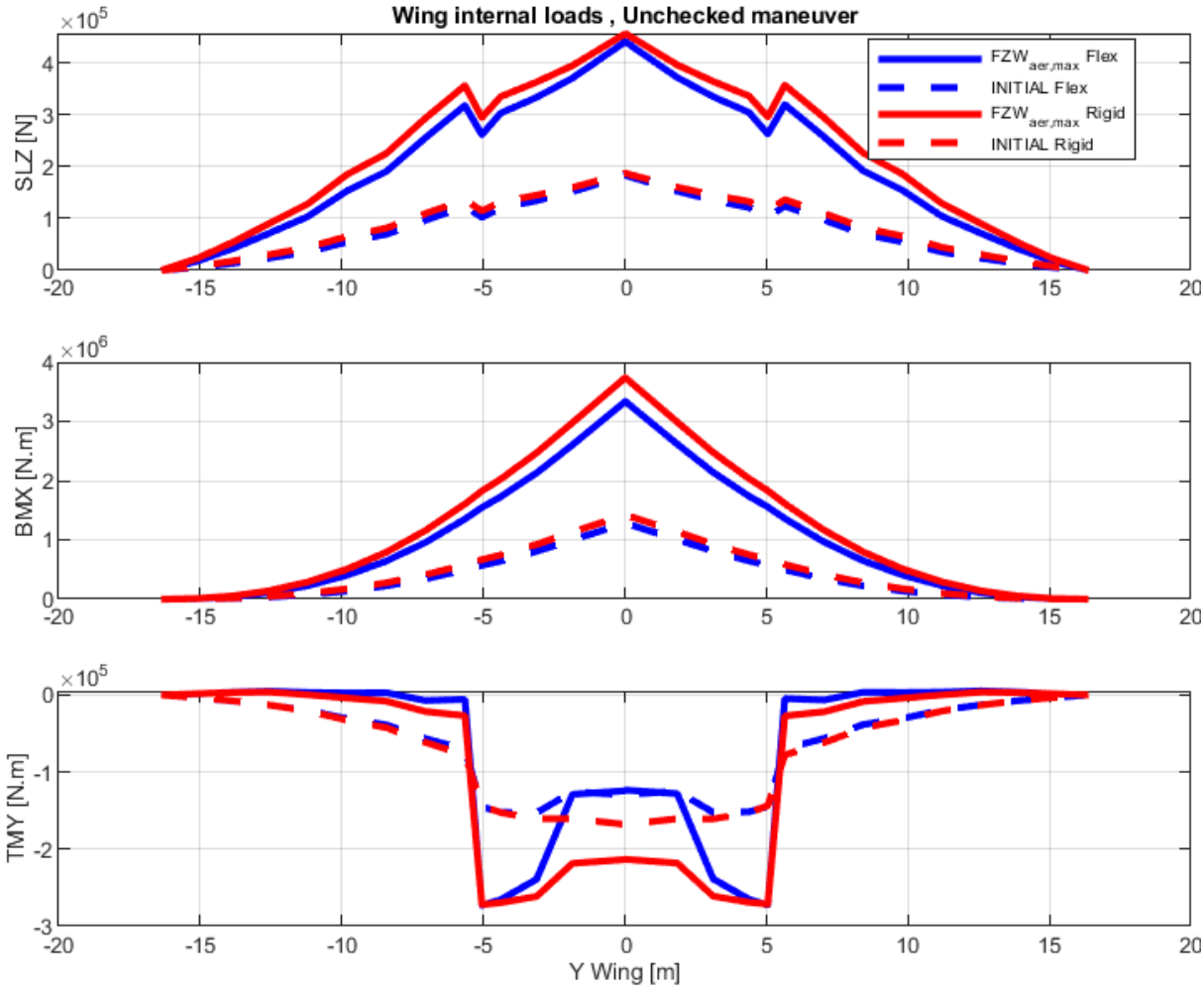


Figure 8: Wing internal loads diagrams for unchecked maneuver simulation

The right side plots present the spanwise distributions of angle of attack and vertical aerodynamic force coefficient. The first plot illustrates the distribution of local angle of attack, which is derived directly from the local velocities within the aerodynamic model. This calculation assumes the average angle of attack for the control points associated with the panels at each station ($\alpha_{local,avg}$). The second plot presents the summation of the $\alpha_{local,avg}$ and the rotation of the wing elastic axis ($\varphi_y$), providing a representation of the relative local angle of attack. This conveys the net angle of attack experienced locally by the wing. The last plot presents the distribution of aerodynamic vertical force coefficient ($CZ$), calculated for each surface station.

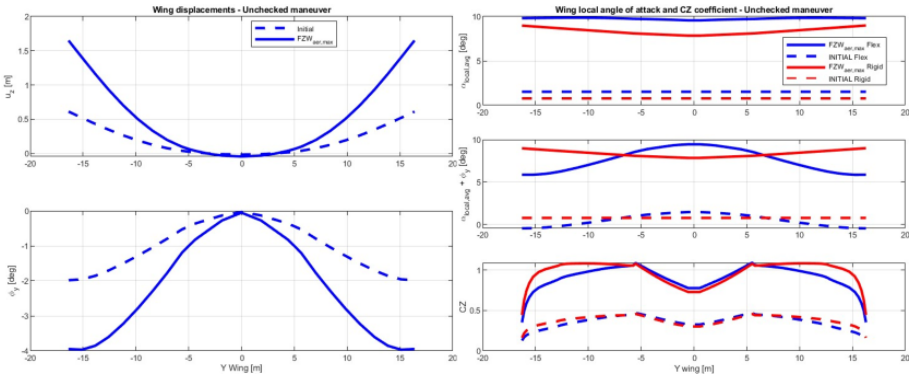


Figure 9: Wing displacements, $\alpha_{local,avg}$ and $CZ$ coefficients for unchecked maneuver simulation

The horizontal tail internal loads diagrams are presented in Figure 10.

Figure 11 presents the plots of horizontal tail elastic axis displacements, angles of attack and aerodynamic $CZ$.

It is observed that the wing and horizontal tail loads of the flexible model consistently exhibit slower values compared to the rigid-body aircraft for the unchecked maneuver.

Specifically, in the case of the wing, the root shear load (SLZ) in the flexible model is approximately 3.4% smaller, and the root bending moment (BMX) is 10.7% smaller than those in the rigid-body model at the moment of maximum aerodynamic vertical force (FZ). These differences can be attributed to several factors. One notable reason is the lower total wing FZ in the flexible model, stemming from a reduced negative horizontal tail vertical force (FZHT). Additionally, a significant factor contributing to this variation is the decreased local angle of attack at stations closer to the wingtip, primarily influenced by torsional displacement of the wing. The primary cause of this nose-down displacement is positive bending of stations near the wingtip, inducing a nose-down torsion moment at stations closer to the wing root. In the case of the torsion moment (TMY), larger differences between the flexible and rigid models are observed in certain stations due to inertial coupling effects caused by large concentrated masses distant from the elastic axis.

As for the horizontal tail, the flexible model's root SLZ is approximately 15.2% smaller, and the root BMX is 16.1% smaller than the rigid-body model at the instant of maximum aerodynamic FZHT. Since the contribution of elevator deflection is the same for both models, generating high value of negative FZ, the disparities in aerodynamic loads stem from differences in angle of attack, which generates positive FZ. Due to structural displacements, the positive FZ is higher for the flexible model. The root TMY of the flexible model is 3.2% smaller than that of the rigid-body model, with this smaller difference compared to SLZ and BMX attributed to inertial coupling effects.

### 6.2 Checked Maneuver

The checked maneuver is simulated according to CS-25 §25.331(c)(2)(i). The time history of both elevators deflection is calculated according to the following equation [19]:

$$\delta_e(t) = \delta_1 \sin(\omega_{sp} t) \quad for \quad 0 \leq t \leq t_{max} \tag{54}$$

where $\delta_1$ is the maximum amplitude of elevator deflection, $\omega_{sp}$ = 2.07$rad/s$ is the frequency

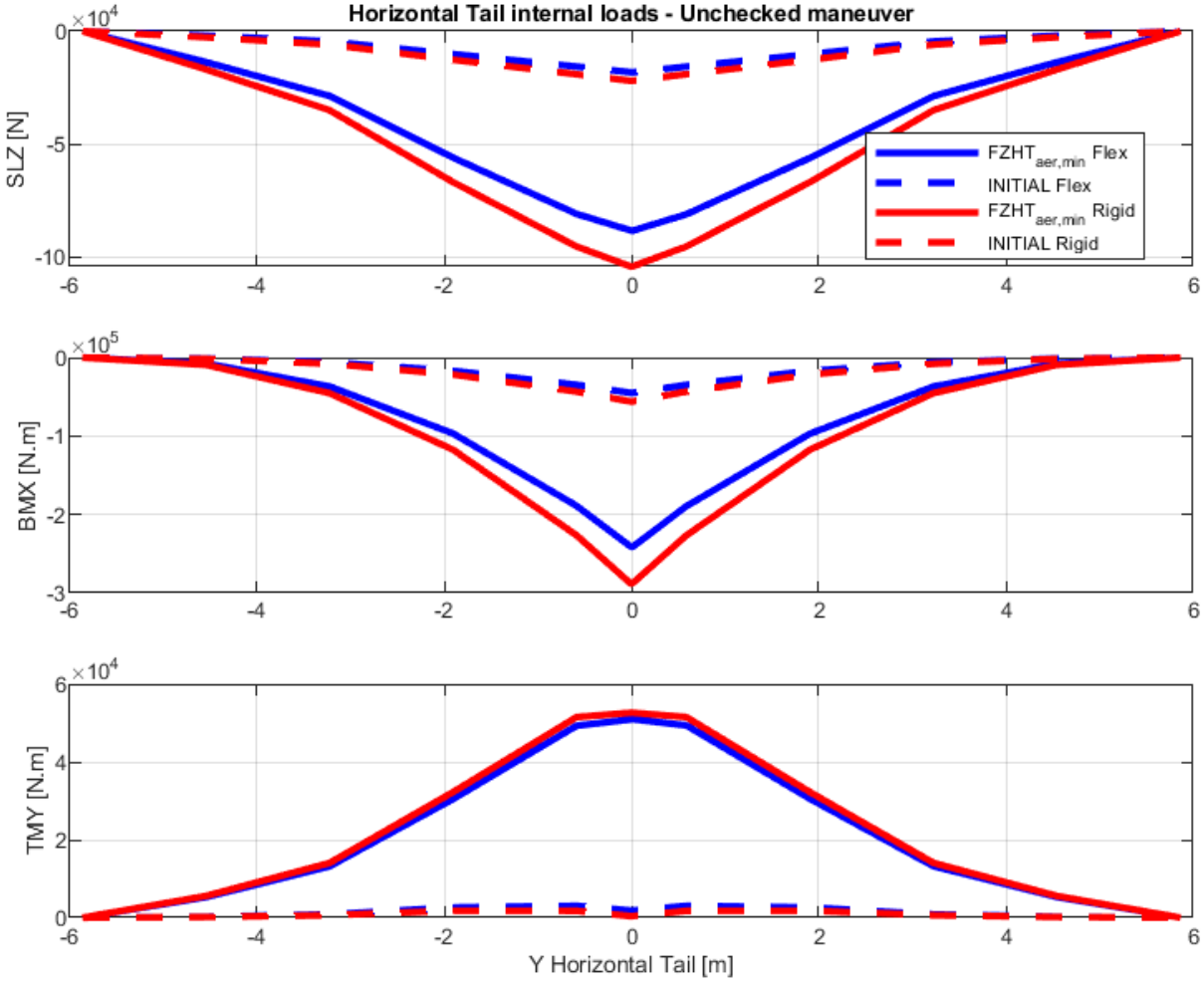


Figure 10: Horizontal tail internal loads diagrams for unchecked maneuver simulation

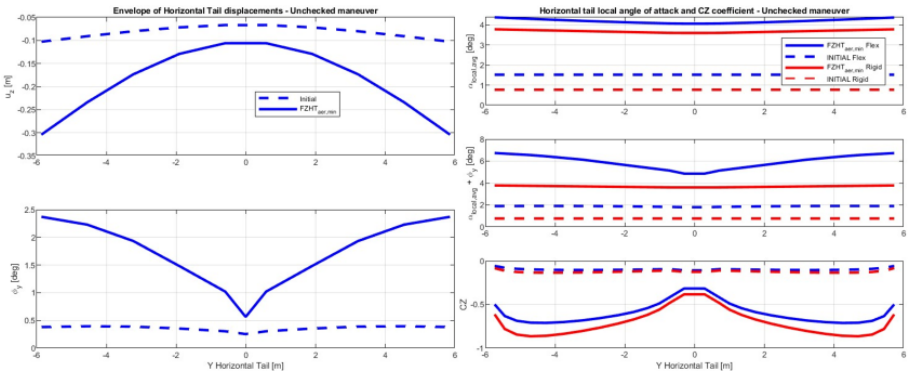


Figure 11: Horizontal tail displacements, $\alpha_{local,avg}$ and $CZ$ coefficients for unchecked maneuver simulation

of the short period rigid mode of the aircraft, and $t_{max} = 3\pi/2\omega_{sp}$. To obtain more consistent comparisons, the value of $\omega_{sp}$ is assumed the same for the rigid and flexible models.

Two simulations of checked maneuver are conducted for each model: the nose-up maneuver, where the sinusoidal elevator deflection has a negative pick deflection at the first half-cycle, resulting in the attainment of the aircraft positive limit load factor, and the nose-down maneuver, where the sinusoidal elevator deflection has a positive pick deflection at the first half-cycle, leading to the achievement of $N_Z = 0$.

### *6.2.1 Checked Maneuver - Nose-Up*

Figure 12 presents the time histories of the nose-up checked maneuver control variables and the response of translational and rotational accelerations. For the flexible aircraft model, the value of $\delta_1$ obtained for the simulation is equal to -10°, and for the rigid-body model, $\delta_1$ = -9°.

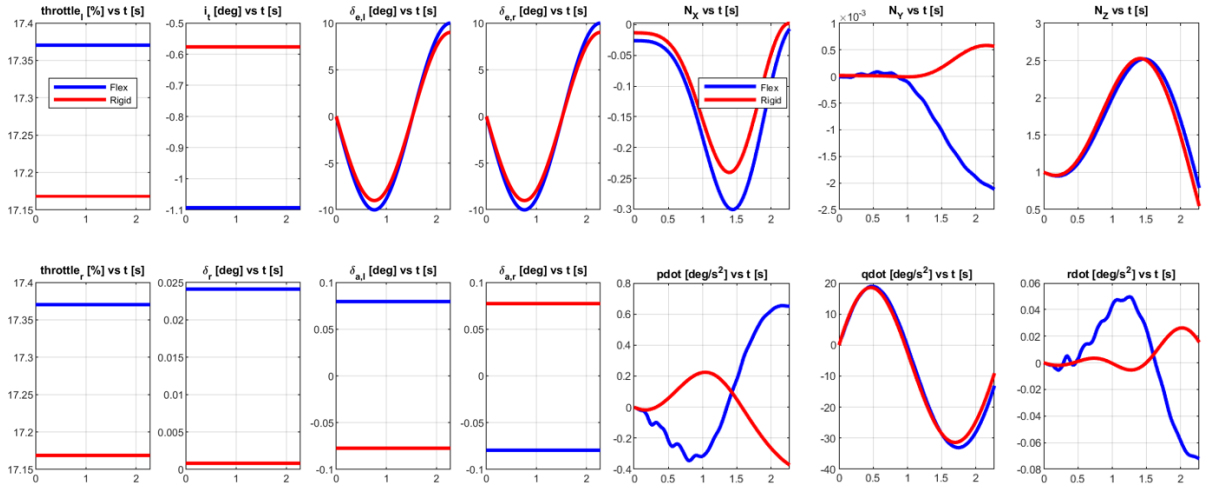


Figure 12: Time history of control variables and accelerations for nose-up checked maneuver simulation

The time history of wing, horizontal and vertical tails aerodynamic and total forces are presented in Figure 13.

For the wing comparisons, only the instant of maximum vertical aerodynamic force $FZW_{aer,max}$ is selected. The wing internal loads diagram for this instant is presented in Figure 14.

Figure 15 presents the plots of wing elastic axis displacements, the spanwise distributions of angle of attack and vertical aerodynamic force coefficient.

The horizontal tail internal loads diagrams are presented in Figure 16, considering two different instants: the instant of maximum positive aerodynamic vertical force at the horizontal tail ($FZHT_{aer,max}$) and the instant of maximum negative aerodynamic vertical force at the horizontal tail ($FZHT_{aer,min}$).

Figure 17 presents the plots of horizontal tail elastic axis displacements, angles of attack and aerodynamic $CZ$.

### *6.2.2 Checked Maneuver - Nose-Down*

Figure 18 presents the time histories of the nose-down checked maneuver control variables and the response of translational and rotational accelerations. For the flexible aircraft model, the

value of $\delta_1$ obtained for the simulation (see Equation 54) is equal to 6.0°, and for the rigid-body

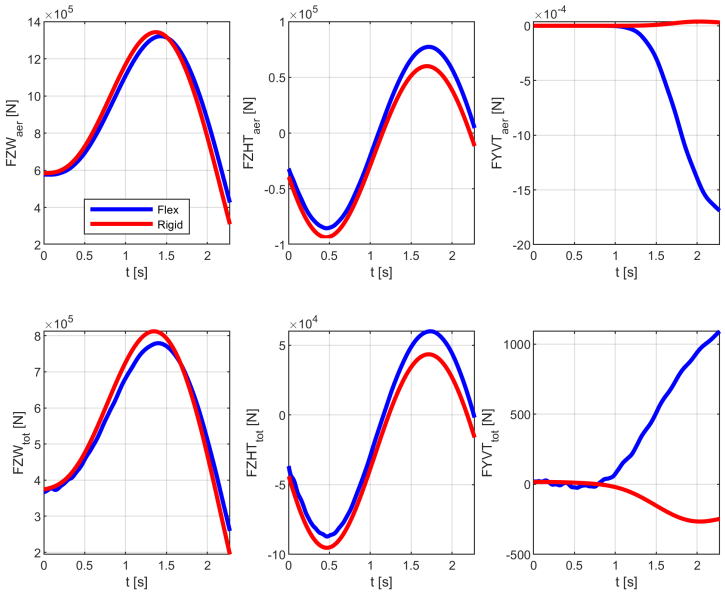


Figure 13: Time history of component forces for nose-up checked maneuver simulation

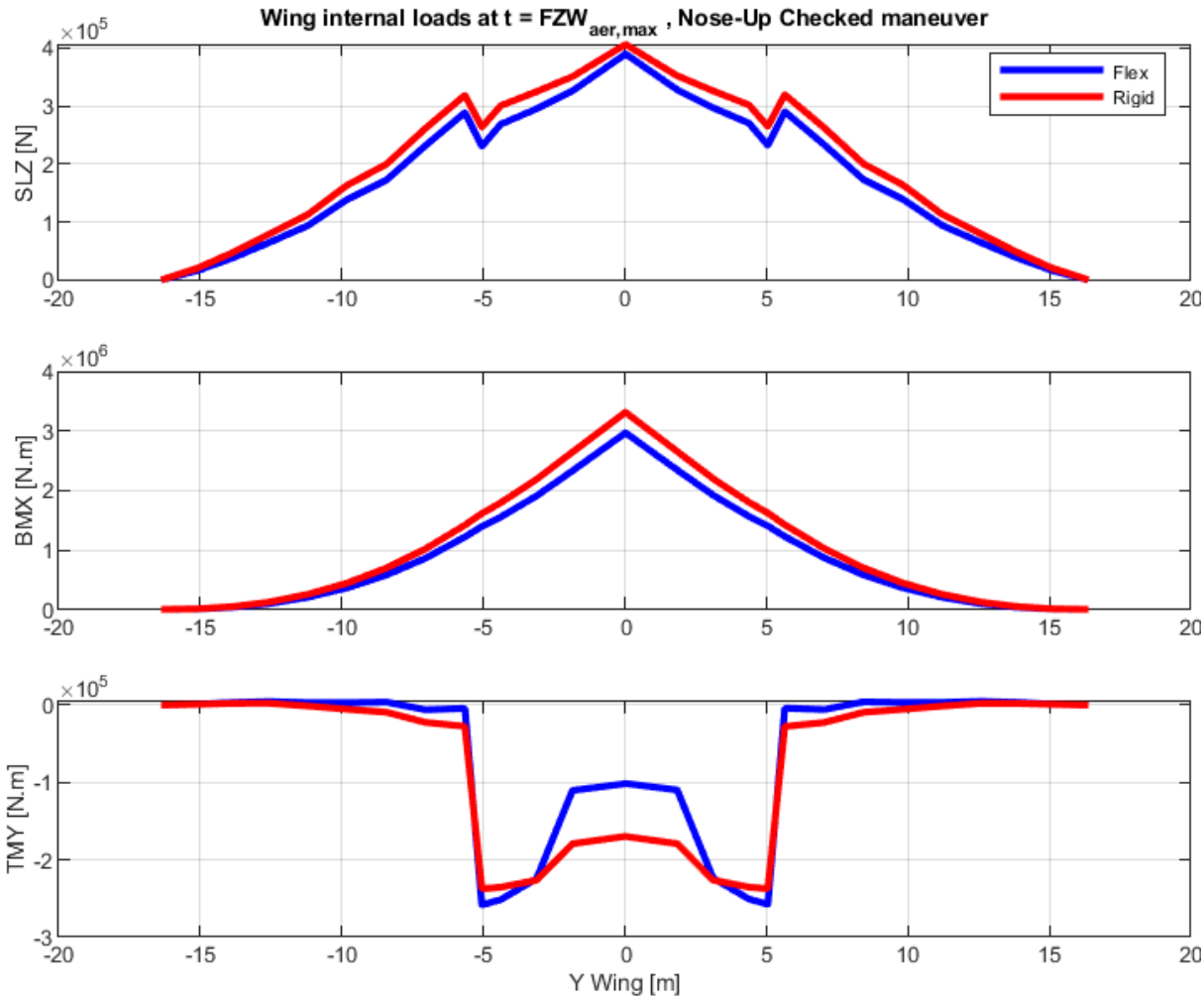


Figure 14: Wing internal loads diagrams for nose-up checked maneuver simulation

model, $\delta_1 = 5.4°$.

The time history of wing, horizontal and vertical tails aerodynamic and total forces are presented in Figure 19.

From Figure 19, it is noted that the wing total FZ from both models is very similar. Therefore, presenting the internal loads diagram will not contribute to any conclusion different from the ones already presented for the nose-up checked maneuver.

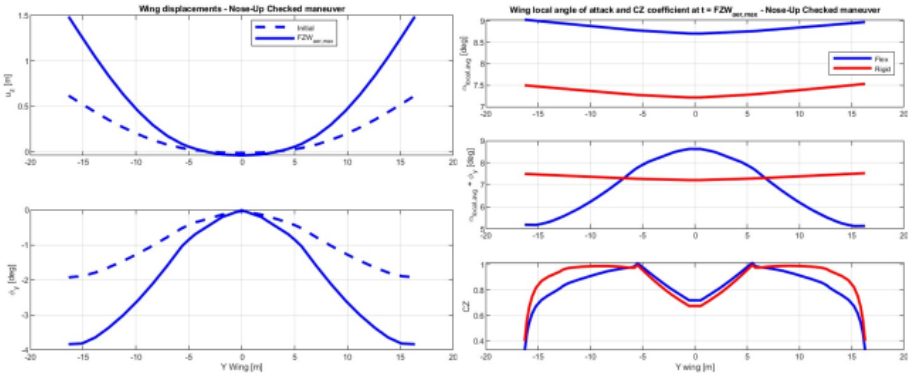


Figure 15: Wing displacements, $\alpha_{local,avg}$ and $CZ$ coefficients for nose-up checked maneuver simulation

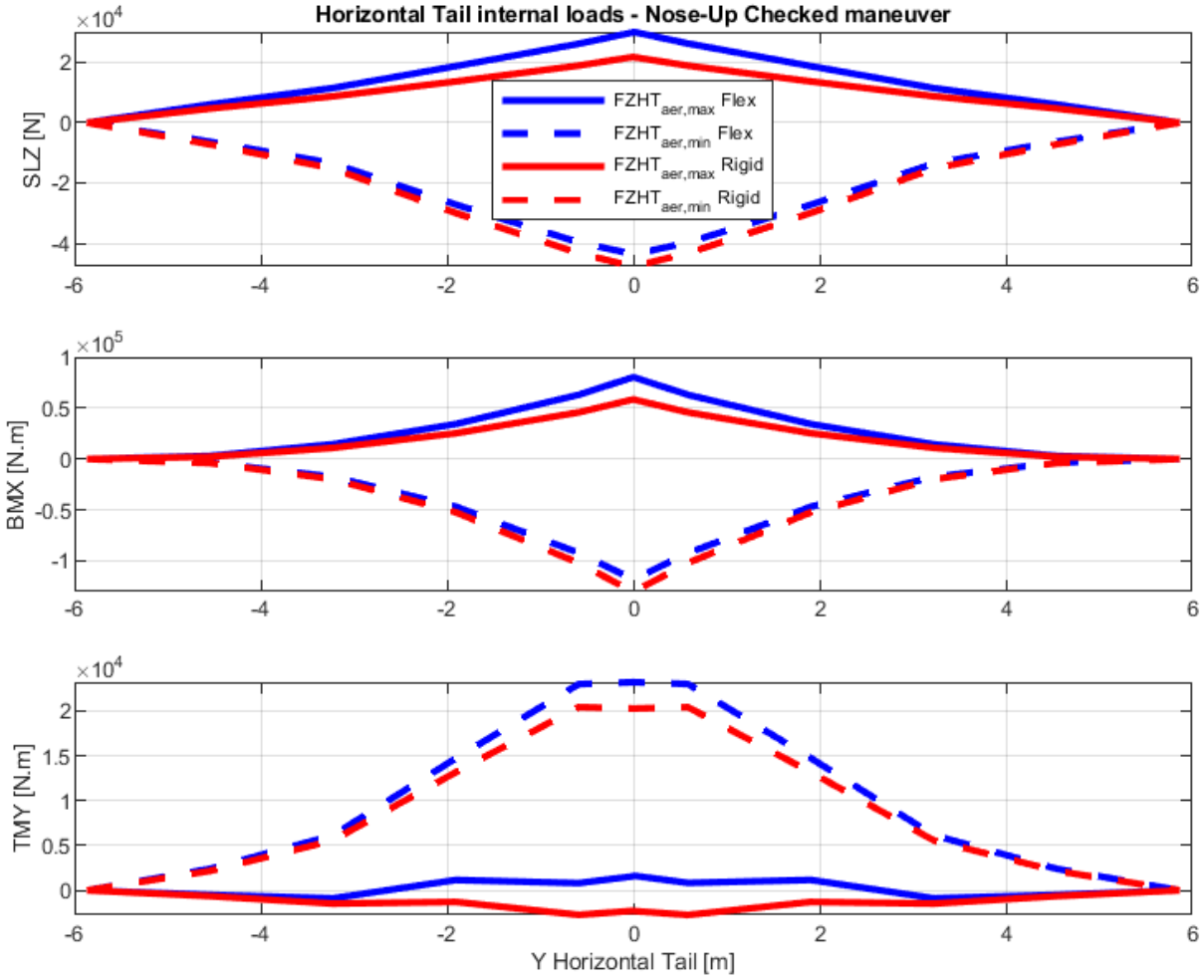


Figure 16: Horizontal tail internal loads diagrams for nose-up checked maneuver simulation

The horizontal tail internal loads diagrams are presented in Figure 20, considering the instant of maximum positive aerodynamic vertical force at the horizontal tail ($FZHT_{aer,max}$) and the instant of maximum negative aerodynamic vertical force at the horizontal tail ($FZHT_{aer,min}$).

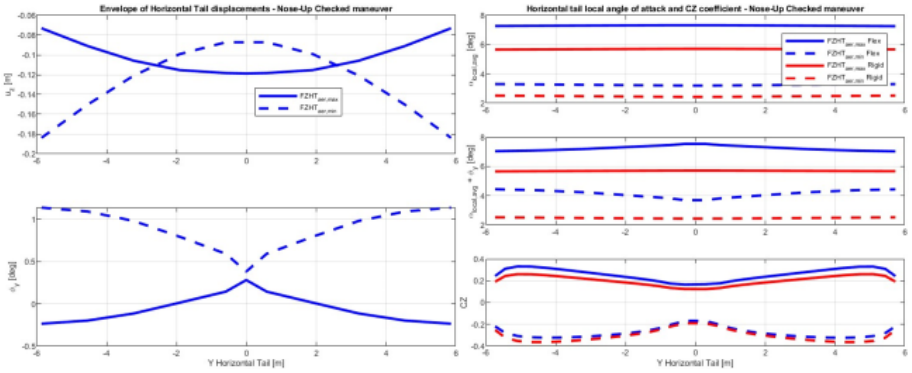


Figure 17: Horizontal tail displacements, $\alpha_{local,avg}$ and $CZ$ coefficients for nose-up checked maneuver simulation

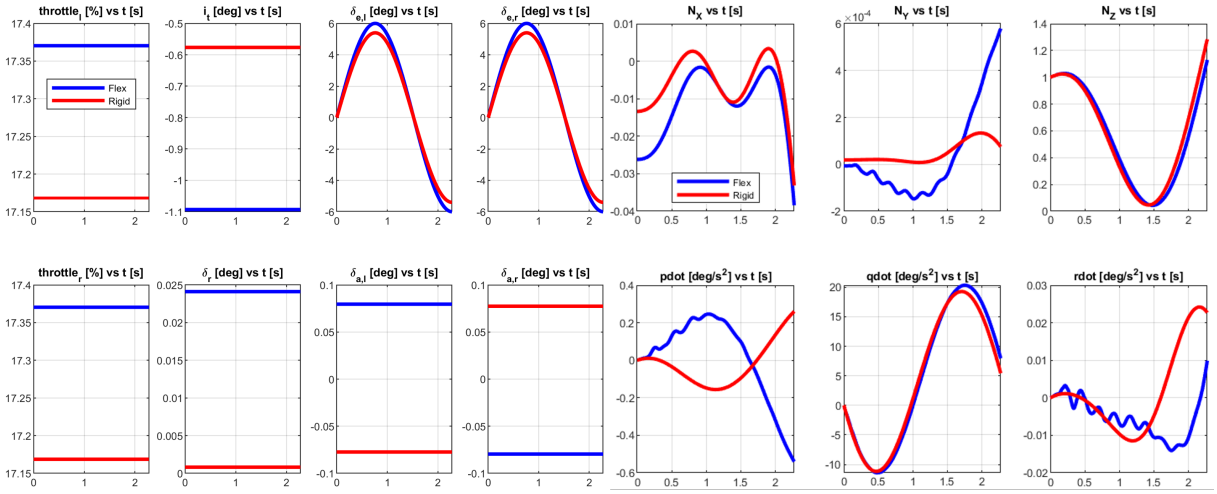


Figure 18: Time history of control variables and accelerations for nose-down checked maneuver simulation

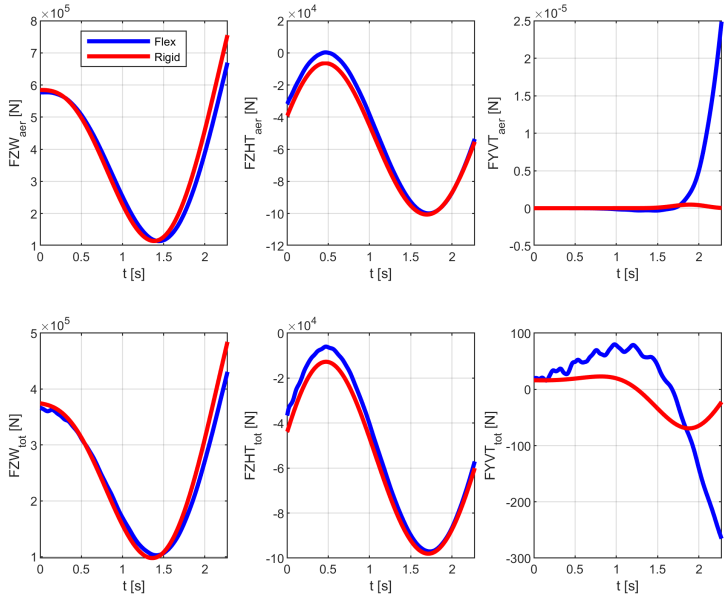


Figure 19: Time history of component forces for nose-down checked maneuver simulation

Figure 21 presents the plots of horizontal tail elastic axis displacements, angles of attack and aerodynamic $CZ$.

### *6.2.3 Checked Maneuver - Discussions*

The elevator deflection profile during the checked maneuver exhibits a smoother response compared to the unchecked maneuver, resulting in a less abrupt airplane response. Additionally, the states obtained for both models are closer, as the influence of elastic degrees of freedom (DOF)

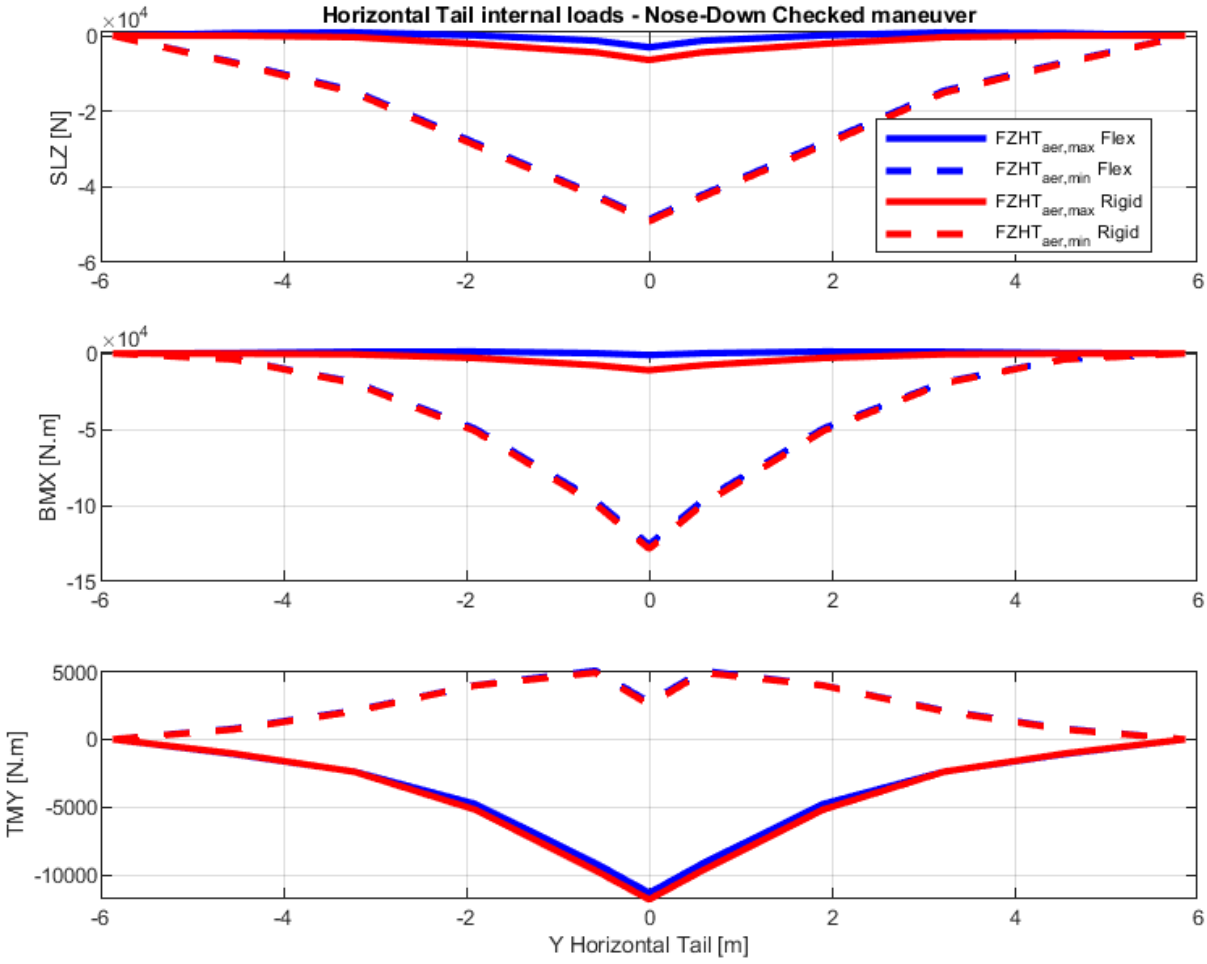


Figure 20: Horizontal tail internal loads diagrams for nose-down checked maneuver simulation

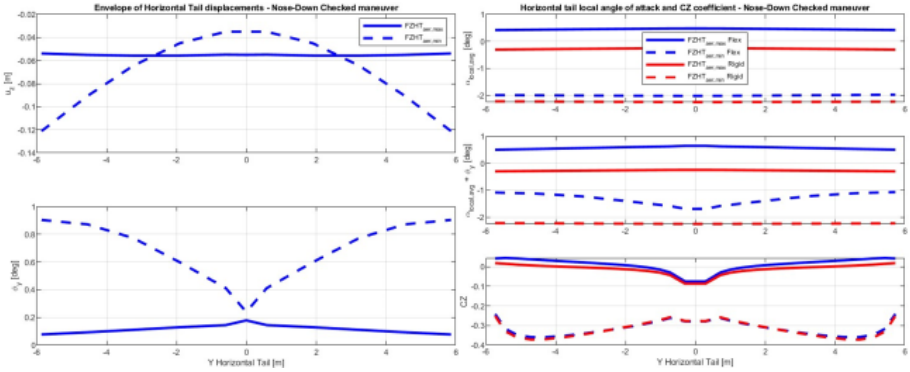

Figure 21: Horizontal tail displacements, $\alpha_{local,avg}$ and $CZ$ coefficients for nose-down checked maneuver simulation

on the rigid-body DOF is reduced.

The behavior of wing loads for the checked maneuver is similar than the obtained for the unchecked maneuver. However, one notable difference arises in the variation of TMY due to large concentrated masses, which is more pronounced in the flexible model compared to the unchecked maneuver. This disparity is attributed to the pitch acceleration at the instant of maximum aerodynamic load ($FZW_{aer,max}$) exhibits an absolute magnitude roughly three times greater than the pitch acceleration in the unchecked maneuver. Consequently, higher torsional loads occur in the flexible model due to inertial coupling effects, as both the rates of structural deformation ($\mathbf{\Phi}_i\dot{\boldsymbol{\eta}}$) and acceleration ($\mathbf{\Phi}_i\ddot{\boldsymbol{\eta}}$) are elevated.

In the case of the horizontal tail, the negative SLZ and BMX loads obtained from both checked maneuvers are higher for the rigid-body model at the instant of maximum negative aerodynamic FZHT. However, the positive SLZ, BMX, and TMY are higher for the flexible model.

The reduced values of negative SLZ and BMX loads in the flexible model (up to 8.5% and 9.3% at the root, respectively) can be attributed to a smaller total aerodynamic FZ, primarily generated by a higher relative angle of attack resulting from structural displacements in the flexible model. Elevator displacements contribute nearly identically, while the contribution of inertial loads remains very similar. Additionally, the 13.6% higher positive TMY for the flexible model at the same instant is due to the higher local angle of attack induced by torsional displacements, leading to increased positive aerodynamic MY, as well as higher inertial loads induced by inertial coupling effects.

At the instant of maximum aerodynamic FZHT of the nose-up maneuver, the root SLZ is 38.2% higher and the root BMX is 37.4% higher for the flexible model, while TMY values are close to zero in both models. These elevated loads in the flexible model are a result of slightly higher positive elevator deflection and local relative angle of attack, induced by structural displacements. The TMY values close to zero are generated by aerodynamic and inertial contributions with similar magnitudes but opposite signs. During the nose-down maneuver, the instant of maximum FZHT exhibits very small SLZ and BMX values but higher TMY values in both models. This combination arises from positive elevator deflection and a local angle of attack nearing zero, resulting in a positive $\Delta C_p$ distribution behind the elastic axis and a negative $\Delta C_p$ distribution ahead of the elastic axis.

### 6.3 Roll Maneuver

The roll maneuver is simulated in accordance with CS-25 §25.349(a) guidelines. During this simulation, both ailerons are deflected from their neutral position to the control stop at a fixed rate of 60°/s. The right aileron is deflected positively, while the left aileron is deflected negatively. The assumed range of aileron deflection is $\pm 20°$. The ramp of aileron deflection starts at the first time step of the simulation, and once the control stop is reached, the maximum aileron deflection is maintained throughout the remainder of the simulation.

The roll maneuver simulation concludes when the increase in roll rate compared to the previous time step ($\Delta p$) falls below 0.01°/s. This condition represents the attainment of a steady roll rate.

While CS-25 §25.349(a) specifies that the roll maneuver should be analyzed in conjunction with a vertical load factor ($N_Z$) of both zero and two-thirds of the limit positive maneuvering load factor (established as 2.5 for the GNBA aircraft in this study), the roll maneuvers conducted in

this research deviate from this guideline. Instead, these maneuvers are initiated from the same trimmed straight flight condition as the previously presented maneuvers, where $N_Z$ is equal to 1.0. The rationale behind this approach is to isolate the influence of the rolling motion, creating more consistent comparisons between flexible and rigid models during a roll maneuver.

Figure 22 presents the time histories of the roll maneuver control variables and the response of translational and rotational accelerations.

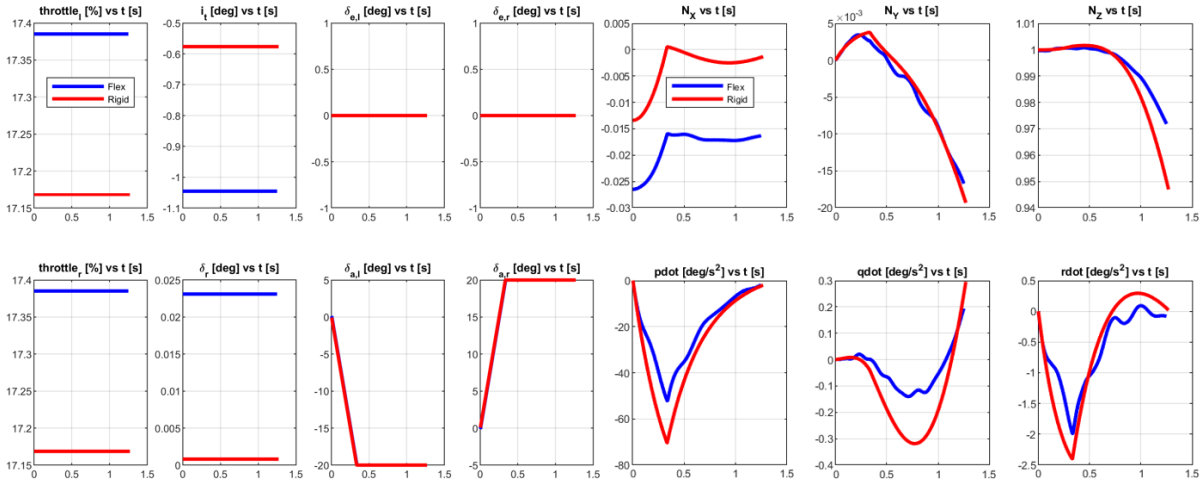


Figure 22: Time history of control variables and accelerations for roll maneuver simulation

Figure 23 presents the time histories of the six lateral-directional states, the relative speed and some relevant aerodynamic parameters and coefficients.

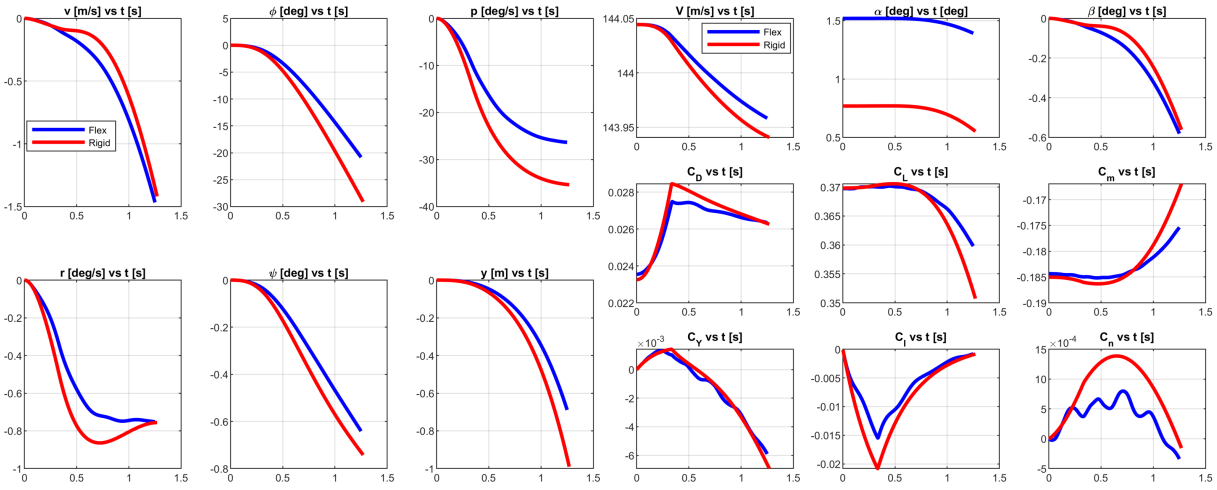


Figure 23: Time history of lateral-directional states and aerodynamic parameters for roll maneuver simulation

In this specific maneuver, the focus of the investigation is solely on the wing's internal loads. Throughout the maneuver, there are no elevator deflections, and the angle of attack remains relatively constant. Consequently, it is not anticipated that any relevant result will arise from an analysis of the horizontal tail's loads.

For the wing comparisons, two instants are defined. The first one is the instant of maximum roll acceleration ($\dot{p}_{max}$), which is the same instant of maximum wing root BMX and TMY, and

also maximum difference between left and right wing root TMY. The second instant is when the maximum roll rate ($p_{max}$) is attained, which is the same instant of the end of the simulation.

The wing internal loads diagrams for these instants are presented in Figure 24.

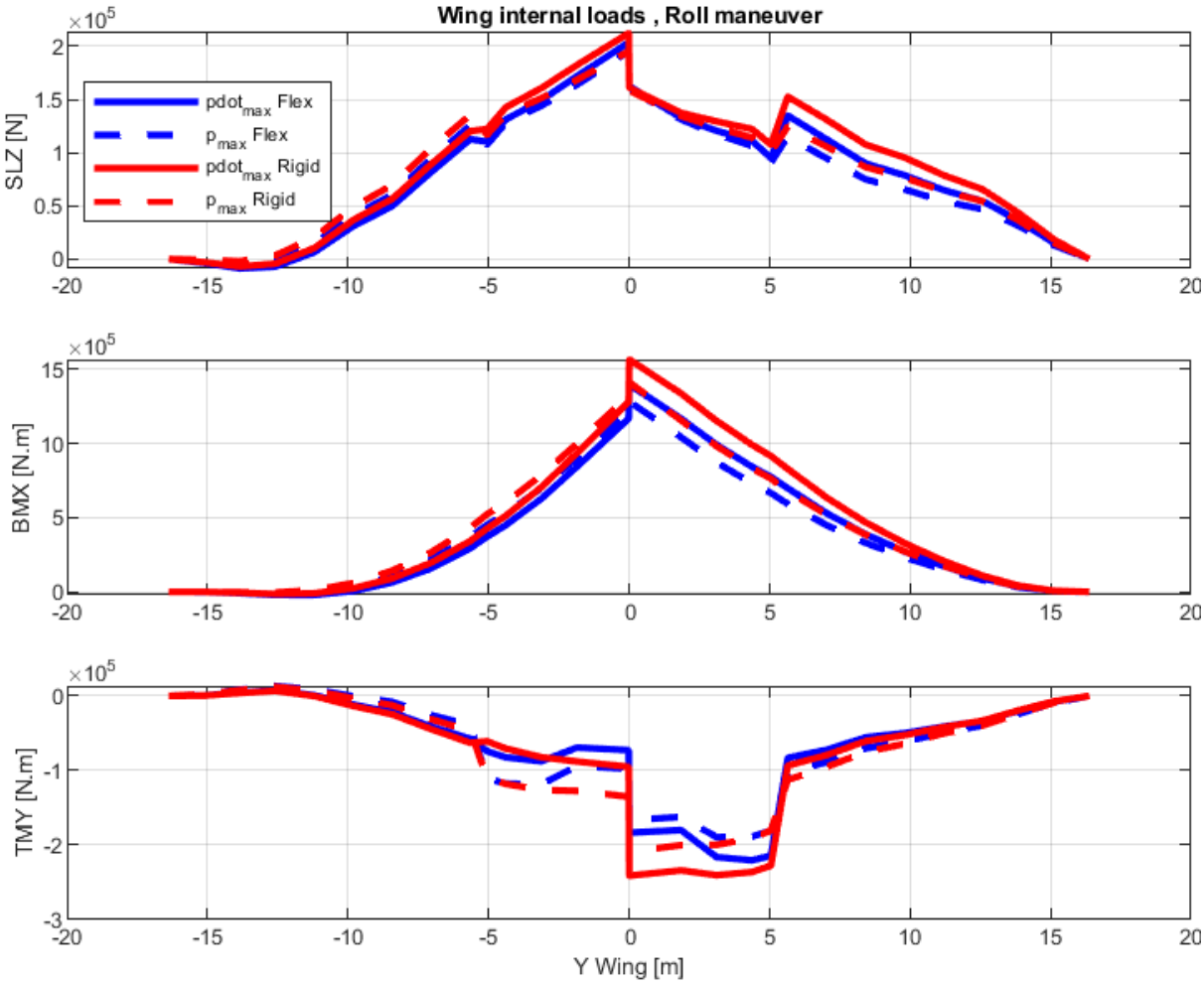


Figure 24: Wing internal loads diagrams for roll maneuver simulation

Figure 25 presents the plots of wing elastic axis displacements, the spanwise distributions of angle of attack and vertical aerodynamic force coefficient.

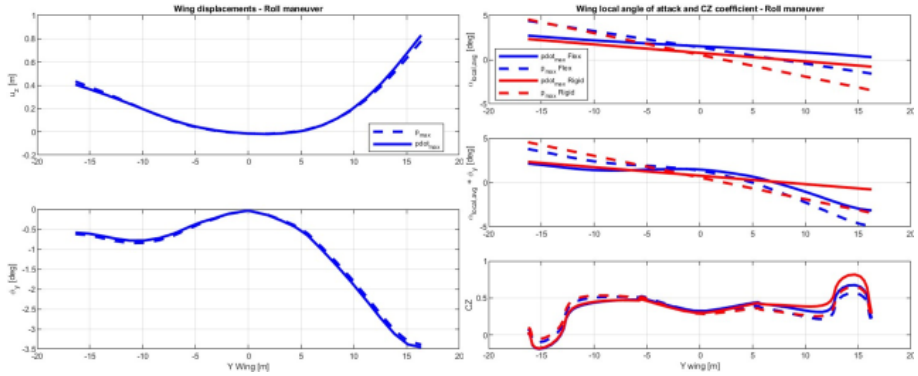

Figure 25: Wing displacements, $\alpha_{local,avg}$ and $CZ$ coefficients for roll maneuver simulation

During the roll maneuver, the wing loads calculated using the rigid-body model consistently

surpass those of the flexible model. The flexible aircraft demonstrates a slower response to abrupt aileron commands compared to the rigid aircraft, resulting in reduced roll rates and accelerations, thus leading to lower inertial and aerodynamic loads during the roll maneuver.

At the instant of maximum roll acceleration, the maximum wing SLZ, BMX, and TMY loads are 4.1%, 10.8%, and 8.6% lower for the flexible model, respectively. These variances primarily stem from higher local FZ at stations farther from the wing root in the rigid model. Structural displacements in the flexible model cause relative angle of attack to be more negative at outboard stations, resulting in lower FZ, while it becomes more positive at inboard stations, leading to higher FZ. Negative torsional displacements are induced by the combination of the wing's positive sweep-back angle and torsion induced by aileron deflection. Due to lower aerodynamic FZ at outboard stations and higher aerodynamic FZ at inboard stations at the instant of maximum roll rate, the maximum SLZ obtained from both models are nearly identical. However, BMX and TMY are 9.1% and 9.3% smaller, respectively.

## 7 CONCLUSION

This study deals with the calculation of flight maneuver loads using a flexible and rigid-body flight dynamic models. The main objective is to compare internal load diagrams of the wing and horizontal tail at identical instants during the same maneuver, derived from both models. The GNBA (*generic narrow-body airliner*) is employed as a platform for the loads analysis.

The framework developed herein for the flight load analysis of an aeroelastic vehicle is valid only when small structural displacements are involved, therefore, it is not suited for highly flexible aircraft.

In the flight maneuvers examined in this study, the wing loads computed with the rigid-body model consistently surpass those obtained with the flexible model, suggesting that the rigid-body model tends to be conservative in estimating wing loads for flight maneuvers.

The nose-up checked maneuver revealed that the rigid-body model is not conservative under all conditions encountered during flight maneuver load analysis. The highest absolute values of horizontal tail SLZ and BMX loads occur at the instant of maximum negative FZHT, with the rigid-body model yielding higher values than the flexible formulation. However, the flexible model demonstrates higher absolute TMY values, while the SLZ and BMX loads at the instant of maximum positive FZHT are greater for the flexible model.

Hence, depending on the structural layout of the horizontal tail, positive loads may induce different stress distributions than negative loads, and a smaller load with an opposite sign may be more critical for sizing certain structural components.

The primary contribution of this study is to demonstrate that increased structural flexibility in modern aircraft can result in significant differences in flight maneuver loads, contingent upon the formulation employed. Adopting a flexible model may prevent the over-sizing of certain aircraft structural components and mitigate the risk of structural failure in others.

### 7.1 Recommendations for Future Works

The flexible model developed in this study is tailored specifically for calculating flight maneuver loads due to its reliance on a quasi-steady aerodynamic model. Hence, the primary recommendation for future work is to implement an unsteady aerodynamic model within the presented

framework. This would allow a multitude of new applications, such as calculation of gust and turbulence encounter loads and aeroelastic stability analysis.

To assess whether a simpler flexible formulation could yield comparable loads to the model developed herein, comparisons with various types of flexible models commonly used in the aerospace industry could be conducted.

Exploring different frequencies for defining elevator deflection input during the checked maneuver (Equation 54) could yield interesting findings.

Another valuable improvement for this framework would be the integration of a pilot model, that is essential for accurately simulating yaw maneuvers.

Another recommendation for future work is to perform the same loads analysis using a different aircraft, that held a different airframe configuration. Different conclusions may be obtained depending on the airframe configuration.

## ACKNOWLEDGMENTS

This study was funded in part by Finep and Embraer S.A. under the research project "Advanced Studies in Flight Physics and Control" - contract number 01.22.0552.00. We express our gratitude to Prof. Antônio B. Guimarães Neto for teaching the course on flexible aircraft modeling, which was fundamental to the implementation of the codes developed in this article, for preparing the GNBA model used both in the course and in this research, and for his fruitful discussions and assistance.

## 8 REFERENCES

[1] Reschke, C. (2006). *Integrated Flight Loads Modelling and Analysis for Flexible Transport Aircraft*. Ph.D. thesis, University of Stuttgart.

[2] Lomax, T. L. (1996). *Structural Loads Analysis for Commercial Transport Aircraft: Theory and Practice*. Reston: AIAA Education Series.

[3] Oliviera, P. H. I. A. (2006). *Introdução às Cargas nas Aeronaves*. Belo Horizonte: UFMG.

[4] Waszak, M. R. and Schmidt, D. K. (1988). Flight dynamics of aeroelastic vehicles. *Journal of Aircraft*, 25(6), 563–571.

[5] Silvestre, F. J. (2012). *Methodology for Modelling the Dynamics of Flexible, High-Aspect-Ratio Aircraft in the Time Domain for Aeroservoelastic Investigations*. Ph.D. thesis, Techn. Univ., Zugl.: Berlin.

[6] Guimarães Neto, A. B. (2014). *Flight Dynamics of Flexible Aircraft Using General Body Axes: A Theoretical and Computational Study*. Ph.D. thesis, Instituto Tecnológico de Aeronáutica, São José dos Campos.

[7] Howe, D. (2004). *Aircraft Loading and Structural Layout*. Bury St Edmunds: Professional Engineering Publishing.

[8] Bisplinghoff, R. L. and Ashley, H. (1962). *Principles of Aeroelasticity*. New York: Wiley & sons.

[9] Wright, J. R. and Cooper, J. E. (2007). *Introduction to Aircraft Aeroelasticity and Loads*. Chichester: Wiley.

[10] Pototzky, A. S. and Perry, B. (1986). New and existing techniques for dynamic loads analyses of flexible airplanes. *Journal of Aircraft*, 23(4), 340–347.

[11] Kier, T. M. and Looye, G. (2009). Unifying manouvre and gust loads analysis models. In *Proceedings "IFASD 2009"*. International Forum on Aroelasticity and Structural Dynamics.

[12] Lone, M., Lai, C. K., Cooke, A., et al. (2014). Framework for flight loads analysis of trajectory-based manoeuvres with pilot models. *Journal of Aircraft*, 51(2), 637–650.

[13] Ritter, M. and Dillinger, J. (2011). Nonlinear numerical flight dynamics for the prediction of maneuver loads. In *Proceedings "IFASD 2011"*. 15th International Forum on Aeroelasticity and Structural Dynamics.

[14] YANG, C., WANG, L. B., XIE, C. C., et al. (2012). Aeroelastic trim and flight loads analysis of flexible aircraft with large deformations. *Science China Technological Sciences*, 55(10), 2700–2711.

[15] Hedman, S. G. (1966). Vortex lattice method for calculation of quasi steady state loadings on thin elastic wings in subsonic flow. Tech. Rep. FFA Report 105, Aeronautical Research Institute of Sweden.

[16] Albano, E. and Rodden, W. (1969). A doublet-lattice method for calculating lift distributions on oscillating surfaces in subsonic flows. *AIAA Journal*, 7(2), 279–285.

[17] Guimarães Neto, A. B. (2020). *Modeling and Simulation of Flexible Aircraft*. São José dos Campos: Instituto Tecnológico de Aeronáutica. 14 chapters. Lecture notes of the course AB-276.

[18] Schmidt, D. K. (2012). *Modern Flight Dynamics*. New York, NY: McGraw-Hill.

[19] European Union Aviation Safety Agency (2023). Certification specifications and acceptable means of compliance for large aeroplanes cs-25. `https://www.easa.europa.eu/en/document-library/certification-specifications/cs-25-large-aeroplanes`. Accessed: 2024-05-28.

[20] Bismarck-Nasr, M. N. (1999). *Structural Dynamics in Aeronautical Engineering*. Reston: AIAA education series.

[21] Roskam, J. (1997). *Airplane Design*. Lawrence: DAR corporation.

[22] MSC Software, Newport Beach (2018). *MSC Nastran 2018.2 Quick Reference Guide*.

## COPYRIGHT STATEMENT